FORMOSAT-7/COSMIC-2 Program
the STAR Annual Report
2020/05

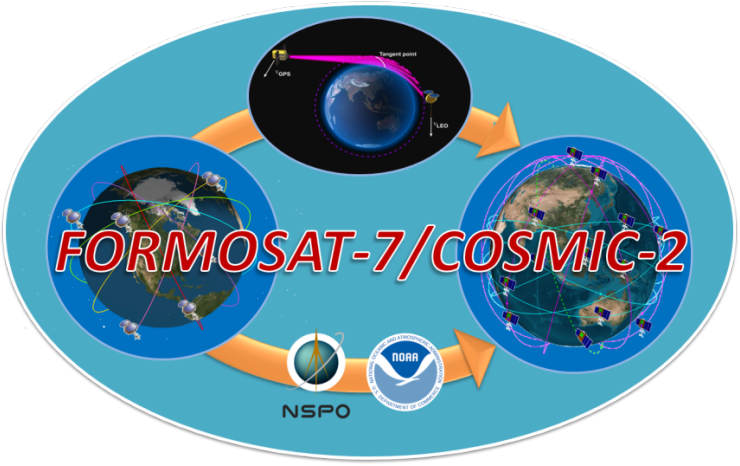

Shu-peng Ben Ho
NOAA/STAR

Main Activities 04/2019 - 4/2020
Submitted May 2018

1. Executive Summary

Radio Occultation (RO) is becoming a core NESDIS observation. Given its importance to NWP, NESDIS decided that radio Occultation (RO) will be a long-term core observable to be treated the same way we treat MW and IR radiances. The general goal for STAR is to build a long-term RO data processing center (PDC) to support all RO related operational and science applications as we do for Microwave and Infrared Sounders.

A COSMIC (Constellation Observing System for Meteorology, Ionosphere, and Climate) follow-on mission, COSMIC-2, has been successfully launched into low-inclination orbits in June 25, 2019. Starting in 2019, the NESDIS OPPA began funding NESDIS/STAR to execute COSMIC-2 related tasks.

Currently, one STAR federal employee leads L1b-L2 processing and validation. STAR is also in the process of hiring another federal employee who will focus on RO L0 – L1b data processing including Commercial Weather Data for RO (CWD-RO), COSMIC-2, and possible Sentinel-6.

There are a number of new projects / programs where STAR is significantly involved in the exploitation of their RO data: these are from partners' missions (KOMPSAT-5, PAZ, Metop, Metop 2nd Gen, Sentinel-6, etc). These projects also improve the STAR's capability in COSMIC-2 data processing and its science applications.

In the past year we have been coordinating with domestic and international partners from RO data operational centers including EUMETSAT, NSPO, WegC, ROM-SAF, NSPO, UCAR, JPL to develop the optimal in-house RO processing algorithms for both COSMIC-2 and CWDP data. CWD-RO is planned to take advantage of the existence of these other projects and the national and international collaborations among the world-leading RO processing centers and operational NWP centers.

In addition, with in house experts of radiosonde data (NPROVS), IR data (NUCAP), and MW data (MiSR), STAR GNSS RO team has demonstrated the CWDP and COSMIC-2 RO validation using available in house developed CrIS, AMT, and RAOB data. Significant contributions by STAR to the Commercial Weather Data Pilot projects in the past two years has provided the foundation for continued work for the next phase of the CWD-RO and COSMIC-2, especially in the in-house expertise to perform satellite (IR/MW) and in situ (radiosonde) inter-comparison to validate the CWD RO and COSMIC-2data, which is essential for the success of NOAA's CWD program and COSMIC-2 program.

STAR has been developed as a GNSS RO processing and research center. Since Sep. 2019, we have developed the STAR GNSS RO Data Processing and Validation System for multiple RO missions. In particular, we have dedicated our efforts on (i) RO data processing (both L1a-L1b

processing, and L1b to L2 processing), (ii) developing the Integrated calibration and validation (cal/val) system (ICVS) for data monitoring, (iii) multi-sensor validation, and (iv) data assimilation.

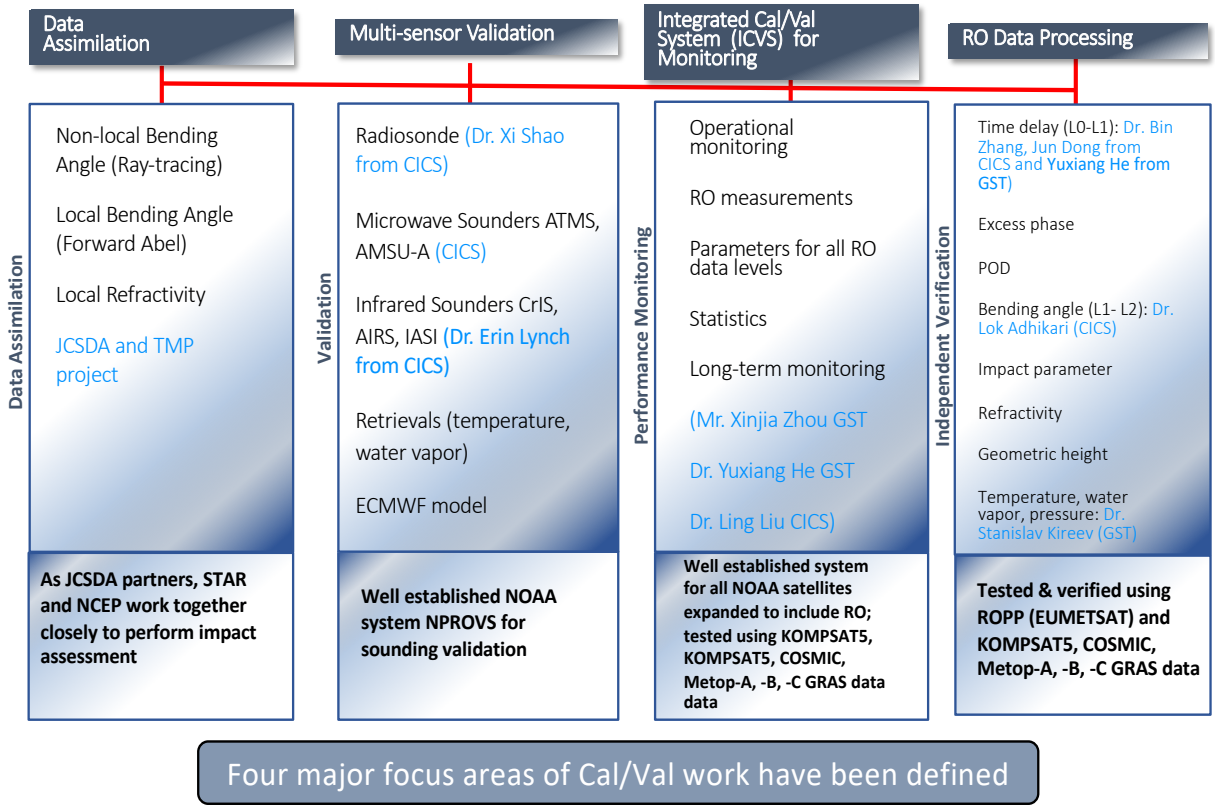

Figure 1. Four major focus areas of STAR COSMIC-2 RO processing and validation system.

In this report we briefly summarize STAR's accomplishments for COSMIC-2 execution include:

1) Development of Stand-alone STAR Excess Phase (L1a-L1b) GNSS RO Inversion Package (Section 2)
2) Development of STAR Stand-alone Bending Angle (L1b-L2) Processing Package (Section 3)
3) Development of STAR 1D-var Algorithm to Derive Temperature and Moisture Profiles in the Neutral Atmosphere (Section 4)
4) STAR ICVS Tool Development (Section 5)
5) Development of STAR Multi-sensor Validation System (Section 6)
6) Highlights of STAR RO Studies and Validation Results (Section 7)
7) Summary of STAR Coordinating Activities, Presentations, and Publications (Section 8)

2. Development of Stand-alone STAR Excess Phase (L1a-L1b) GNSS RO Inversion Package

In this section, we summarize the development of STAR L1a-L1b processing package which provides the steps converting the phase observation (opnGns files) to bending angle (cicPhs files) in Section 2.1. We also and compare our solution with STAR bending angle (BA) profiles with those computed from ERA-5 to understand the differences and errors in excess phase and bending angle products in Section 2.2. The development of L1a – L1b COSMIC-2 processing package is to prepare STAR as RO data processing center (DPC).

2.1 Processing Steps

To derive bending angle and refractivity profile from RO occultation measurements, one must perform L0-L1 (from raw data to excess phase) and L1-L2 (converting excess phase to bending angle) processing. In the past year, STAR GNSS team has developed the capability to perform both L0-L1 and L1-L2 data processing. **Figure 2** depicts the flow chart of the STAR RO processing procedures.

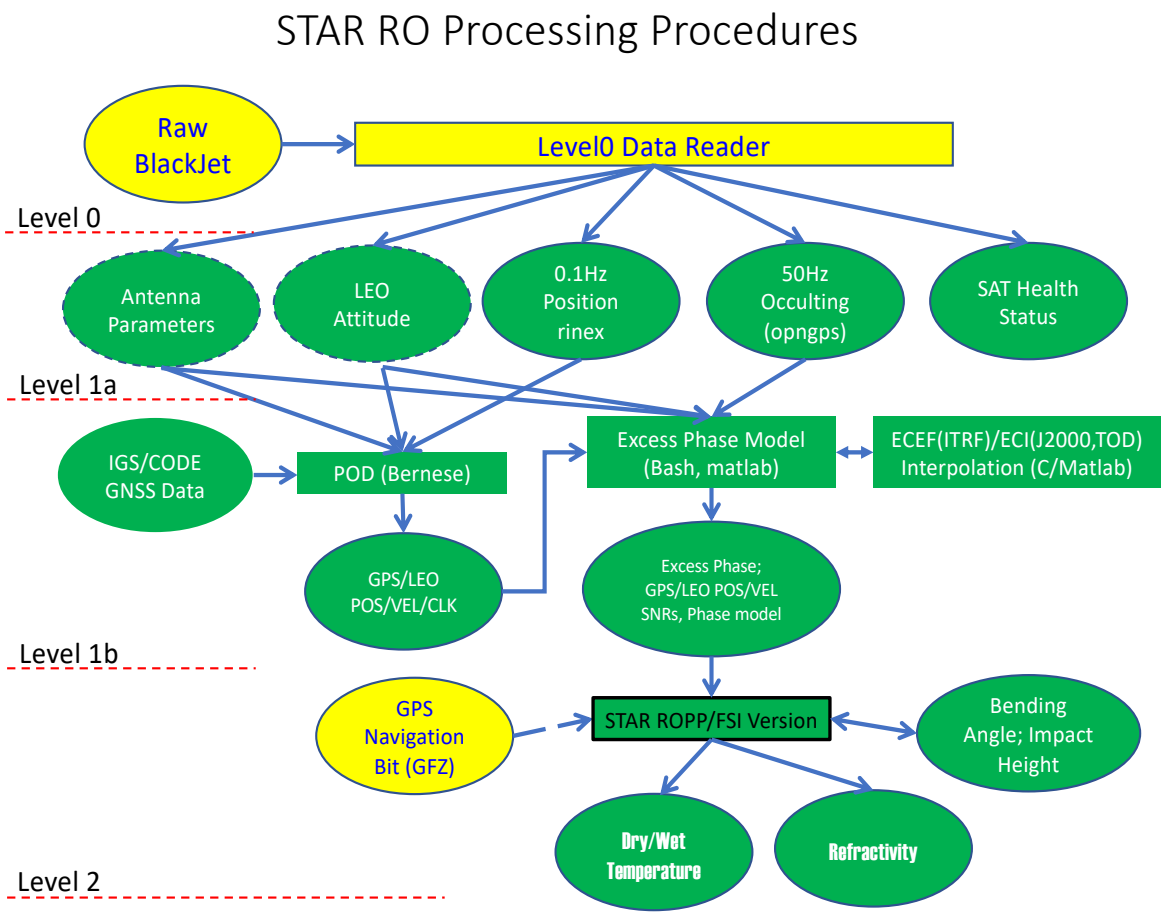

Fig. 2 The flow chart of the STAR RO processing procedures.

For L0-L1 processing, we are able to perform 1) precise orbit determination (POD) and clock synchronization to eliminate the effects of the geometric Doppler and of relative transmitter receiver oscillator drift, 2) bending angle calculation, 3) ionospheric corrections, 4) Abel integral inversion with upper boundary conditions, and 5) quality control (QC).

STAR processing algorithms include the following sequential processing modules (details can be seen in Section 3):

a. ***I/O subroutine*** to read phase, amplitude and geometry data
b. ***Translation subroutine*** to change ECEF coordinates to local center of curvature and calculate the radius of curvature. The Flow chart to calculate the propagation of GPS and LEO orbits to circular orbits relative to a local center of curvature is described in **Fig. 3**.
c. ***Projection subroutine*** to project GNSS/LEO orbit to fixed radii from local center of curvature
d. ***FFT subroutine*** to get bending angle at each impact parameter: This is the core FSI/FFT subroutine.
e. ***Inverse Abel subroutine*** to compute refractivity from bending angle/impact parameter.

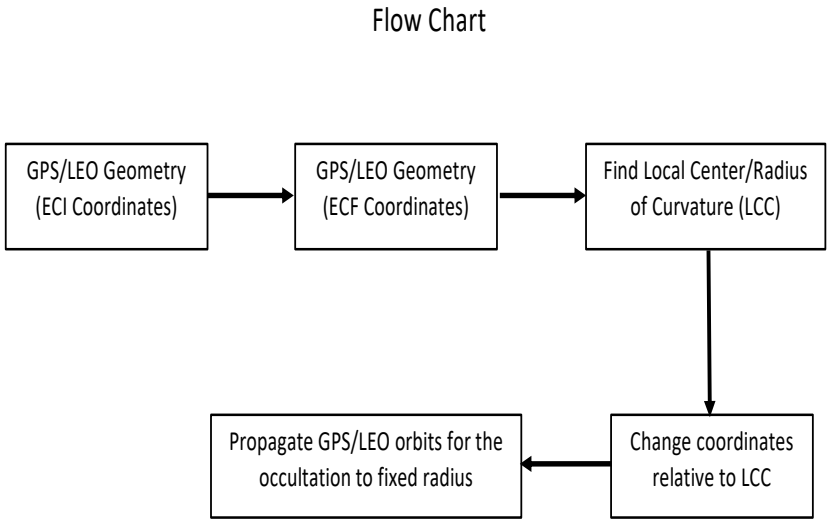

Fig. 3. Flow chart to calculate the propagation of GPS and LEO orbits to circular orbits relative to a local center of curvature.

2.1.1 Extracting the opnGns phase and Rinex file phase

The OpnGns of GeoOptics has 100 HZ observations, approximately 0.02 seconds intervals. Usually the file provides the observations (pseudo range: C1C, L1 Phase: L1C, L2 Phase: L2L, and SNR: S1C,S2C) and modeled phase data (L1C(M) and L2L(M)). One important step in this

opnGNS processing is to extract all the information and concatenate into one formatted file (easily readable into matlab) and determine each Radio Occultation events and their associated start and end time. Based on the RO event starting and ending time, we look into the same day RINEX observations from POD antennas. For each continuous of a single GNSS observation by the POD antenna, we called them a reference link event. The pair between the RO event and a reference link event are determined by looking at the reference link data SNR and its time range covering the RO event.

2.1.2 Orbital Determination for LOE/GNSS position and velocity

The LEO (Geoptics) POD has been provided as SP3-D format with 1HZ interval. At this time, due to the lengthy processing in Bernese, we decided to use the GeoOptics provided L1a POD information. We extract the GPS time, Position and velocity in ECEF and Clock bias from all the SP3-D files in one day and forms a formatted data file into matlab. This step is relatively easy since it only involves the format change. However, we found that the SP3-D orbit has large clock bias. The bias in the time derivatives of the positioning can cause wavy structure in the bending angle profiles. We also looked into the level-2 POD file, cicPOD, which has complete 1HZ POD information. However, the POD position of the LEO satellite is given in ECI coordinate system and we have to do the coordinate transformation.

To derive the GNSS position/velocity and clock information, we have to reply on the CODE/IGS products. The 15 minutes CODE GNSS solution and Earth Orientation Parameters are downloaded/reformatted and feed into the Bernese software. The orbit and clock are reproduced into 30 seconds products using SP3-C format. The SP3-C formats are then used to form formatted inputs to excess phase model to provide the GNSS pos/vel/clk data. For both LEO and GNSS orbit, a high order polynomial interpolation (9^{th} order) has been used in the interpolation of orbital time to observational time.

2.1.3 Extracting the Attitude Information

The GeoOptics attitude file adopts the Champ convention. The quaternions are defined from space craft coordinate to ECI (J2000). We extract the GPS time and the Quaternions into formatted file ready into matlab. Also, the GeoOptics attitude files include the POD and antenna offset information. From here we can derive the antenna offset for POD and excess phase calculation. Together with the SP3/cicPOD file provided GNSS/LEO mass center position, the antenna offset and attitude information can be used to derive the LEO antenna position/velocity in ECI coordinate system.

2.1.4 Earth Coordinate System Conversion

The GNSS/LEO satellite positions are given in ECEF coordinate system with the IGS convention. However, the excess phase calculation involves terms must be corrected in ECI coordinate system. Thus, we need convert the Pos/Vel data sets from ECEF to ECI. While the general coordinate transformation can be done using a generalized matrix considering the earth rotation, the accurate conversion from ECEF to ECI (vice versa) needs a well defined equatorial plane and an earth's pole, where the earth's rotation, precession, nutation and Polar wander must

be considered. Here, we use True of Date coordinate system, one of the ECI, the same as UCAR used for our processing. Before doing the temporal interpolation from POD time (30 seconds interval) to the high rate phase observation time (100 Hz), we carried out the coordinate transformation first, which means the interpolation is done in ECI coordinate system.

2.1.5 Cycle Slip Detection

The cycle slip happens when connecting the observed phase in a range of [- π,+π] to a continuous, unwrapped phase time series. In the discontinuity, an integer number of the (half) wave lengths must be added into the time series; otherwise the time derivative will be changed abruptly and hence affects the bending angle calculation. Generally, the residual phase between the observed L1/L2 phase and phase model are looked. During the phase-locked loop (close) stage, the difference can be easily identified since the change of residual phase between two observational point s are close to zero, hardly exceed quarter of wave length (0.19cm for L1). The integer number of π can be added by minimizing the difference between the previous observation and current. However, during open loop stage, we may also need to reply on the navigation bit time series or an internal NDM correction. Once the phase has been reconnected, it will be added back to the phase model and then provided for excess phase calculation.

2.1.6 Calculation of Excess Phase

We designed an excess phase model (mainly in matlab) to incorporate all steps from coordinate conversion, polynomial interpolation, excess phase calculation and netCDF data output.

The excess phase model can be expressed as the following equation (Figure 4):

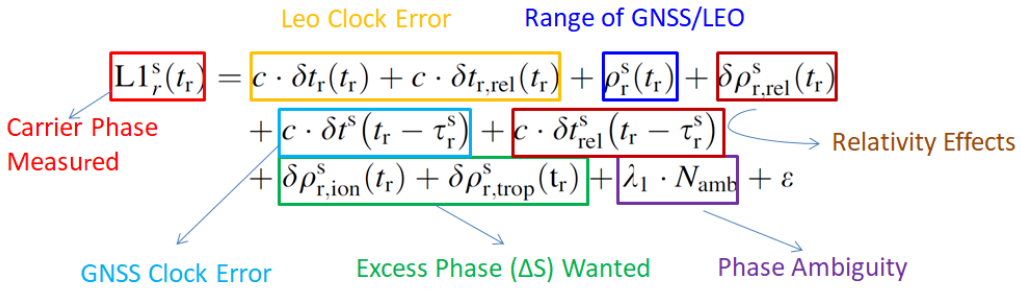

Figure 4. The calculation of excess phase involves different types of phase corrections

From the equation, the dominate part is the LEO clock error. For COSMIC-1, the high rate POD observations can be paired with OCC high rate observations to remove this clock error completely (only increase noise level due to smoothing procedure of L1/L2 phases). For the GNSS clock error, since the GNSS clock is usually very stable (or drift rate is very stable), the error from polynomial interpolation from 30 seconds (or 1HZ GNSS ground station observations) is negligible, a zero differencing can be applied to these parts usually within a few millimeter differences in excess phase. However, we need to estimate the time propagation τ_r^s from the transmitter to receiver. This can be roughly calculated using the direct distance

divided by speed of light and recursively calculated using the GNSS orbit and LEO receive position in ECI coordinate system. The range between transmitter and receiver, $\rho_r^s(t^r)$, refers to the antenna phase center position. Thus, it combines the POD mass center position, the antenna offset and the antenna phase center variation. However, to connect these three, the attitude information must be taken into accounts since the antenna offset and PCVs are given in instrument coordinate system.

It recognized that the POD with accuracy of 10 cm level does not have significant impact on the bending angle calculations, such as COSMIC-1. By examining the POD error in the GeoOptics POD netCDF file, the uncertainty of the POD is on the order of 0.5 cm level (as 1 σ value). Similar to the CLOCK drift, the position error can be easily more than centimeter level. To reduce error, a 10^{th} order polynomial interpolation scheme has been applied to the position and velocity interpolation. The general relativity effects consider time and distance difference when referencing different clocks on different satellites. Those corrections are small but must be done in a inertial system, that's why the excess phase is always associated with position/velocity in the ECI coordinate system.

The basic steps in calculation of excess phase:

1) Determine the high rate OCC time, in 0.01 second interval.
2) NDM removal for residual phase and added back to phase model.
3) Calculate the phase center position/velocity of the LEO satellite receiver and GNSS transmitter at OCC time 10^{th} order polynomial interpolation.
4) Calculate the range of the transmitter and receiver.
5) Subtract the range from both L1/L2 phase.
6) Calculate general relativity terms and subtract these corrections from phase.
7) Calculate the referenced link 1HZ L1/L2 observations from RENIX file and pair with the opn
8) Remove the GNSS clock bias using zero differencing (4^{th} order polynomial interpolation).
9) Apply the same algorithm to 1HZ POD observations and interpolate the results into OCC observation time.
10) Linearly combine L1 and L2 phase from 7) to form L3, the single differencing clock error.
11) Subtract L3 in 6) from residual phase in 4.) and subtract a constant to make the first excess phase value as zero.
12) Format the datasets and output as netcdf as function of GPS time (with bias corrected). The netCDF variables include excess phase, phase model, position and velocity of transmitter and receiver, SNR as function of the GPS time (with bias corrected).

While the steps look straight forward, there are many caveats and subtle steps needing additional care. Such as dealing with the LEO receiver POD/OCC antenna offsets needs the LEO attitude information, dealing with GNSS antenna offsets needs the GNSS attitude information. The accuracy of observational time is also important. With receiver clock bias on the order of ~0.1ms, the range error between transmitter and receiver can be 10 centimeters difference (think of the LEO/GNSS relative movements) if not subtracted from the receiving time.

2.1.7 Calculation of Bending Angle

Once the excess phase and SNR as well as associated position/velocity in ECI have been determined out of excess phase model, we can use the Radio Occultation Processing Package for next step, bending angle conversion. The inputs are solely a netCDF file containing all the excess phase related information and a parameter control file. **Figure 5** shows one case of the bending angle profiles using the SP3-D and cicPOD files. We notice that the SP3-D files can cause large errors in the BA, while using cicPOD can result in better solution in bending angle, which is very close to GeoOptics bending angle.

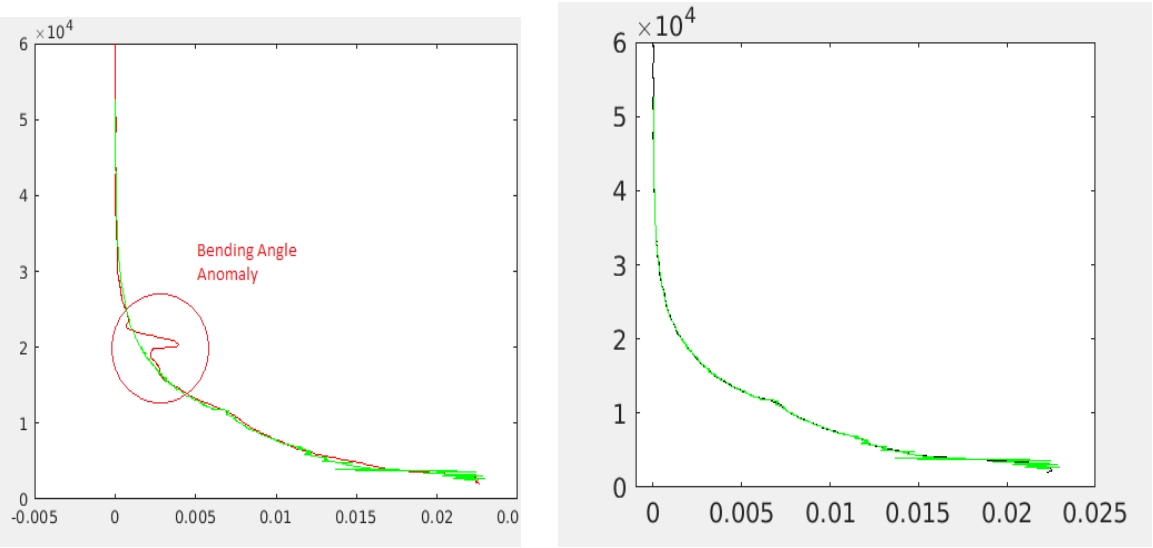

Figure 5. Bending Angle Profiles using GeoOptics SP3-D (left) and cicPOD orbit products.

2.2 Comparisons STAR BA with ERA-5 BA Profiles

Accurate bending angle processed from the raw GNSS signals received from the RO receivers are critical for numerical weather prediction (NWP) through data assimilation (DA). Using STAR inversion package described above, we have successfully inversed the raw phase, amplitude and geometry data provided from COSMIC-2 (and CWDP data) to bending angle profiles.

For the COSMIC-2 data operation, we input the Phase/SNR (signal noise ratio) data and the position and velocity information from UCAR to compute the STAR bending angel (BA) profiles. **Figure 6** depicts the STAR bending angle profiles (processed by UMD – the STAR collaborative institute) compared to the exactly the collocated BA profiles generated using ERA-5. The panel on the left shows the BA profiles generated by UMD (the red lines) and the ERA-5 BA profiles (green lines). The right panel depicts the fractional difference of UMD BA And ERA-5 BA. **Fig. 6** shows that the UMD STAR bending angle are very close to those of ERA-5 with less than 0.1% of fractional difference. The standard deviation of the mean difference (the dashed lines) for UMD-ERA-5 pairs are reasonably small. COSMIC-2 data from 2019 275-301 are used.

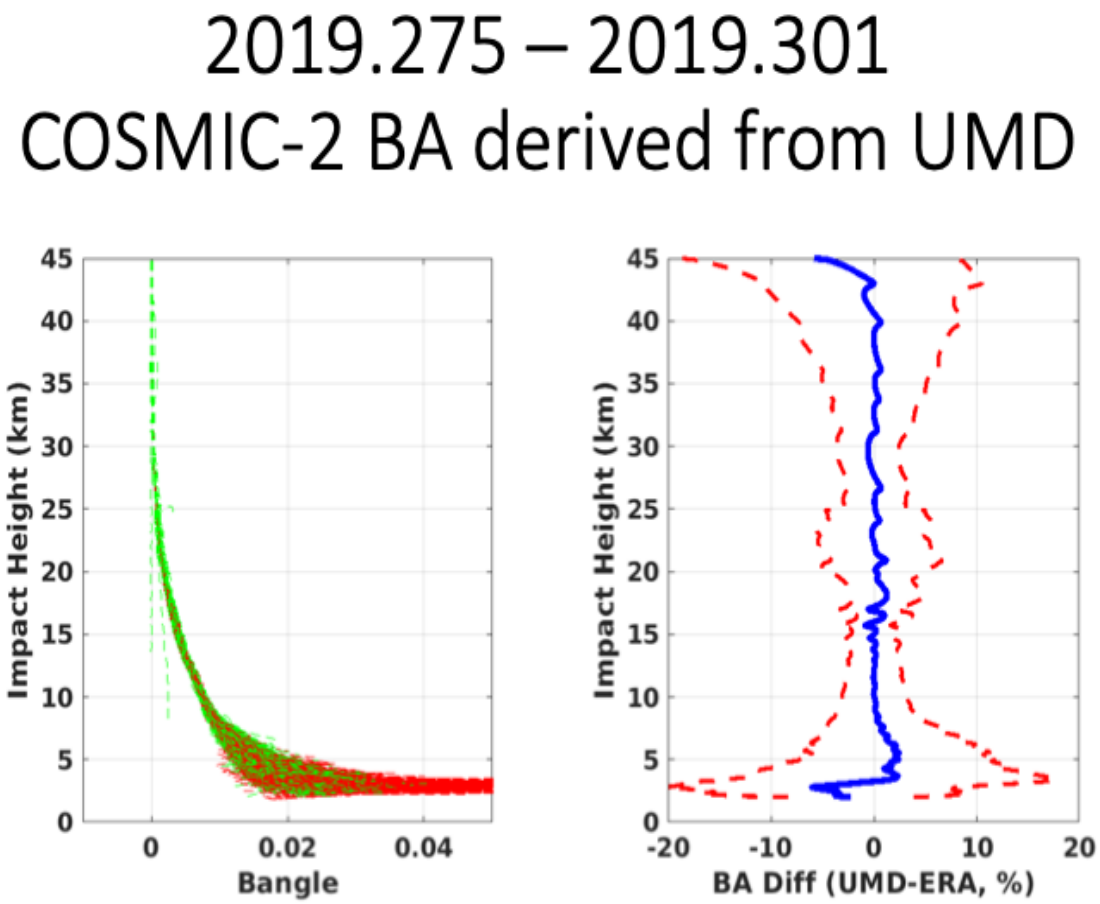

Figure 6. Bending angle profiles difference between STAR and ERA-5 pairs. The panel on the left are showing the BA profiles generated by UMD (the red lines) and the ERA-5 BA profiles (green lines). The right panel depicts the fractional difference of UMD BA And ERA-5 BA.

3. Development of STAR Stand-alone Full Spectrum Inversion (FSI) Bending Angle (L1b-L2) Processing Package

Accurate bending angle processed from the raw GNSS signals received from the RO receivers are critical for numerical weather prediction (NWP) through data assimilation (DA). Using STAR inversion package described above, we have successfully inversed the raw phase, amplitude and geometry data provided from COSMIC-2 (and GeoOptics/SPIRE) to bending angle profiles (i.e., STAR bending angle profiles).

In STAR we develop the stand-alone FSI inversion package to invert COSMIC-2 excess phases into bending angle and refractivity profiles in the neutral atmosphere.

3.1 Inversion Procedures

Figure 7 shows flowchart of the steps used in the Inversion system. Description of each steps are provided in the proceeding sub-sections. **Table 1** shows the implementation.

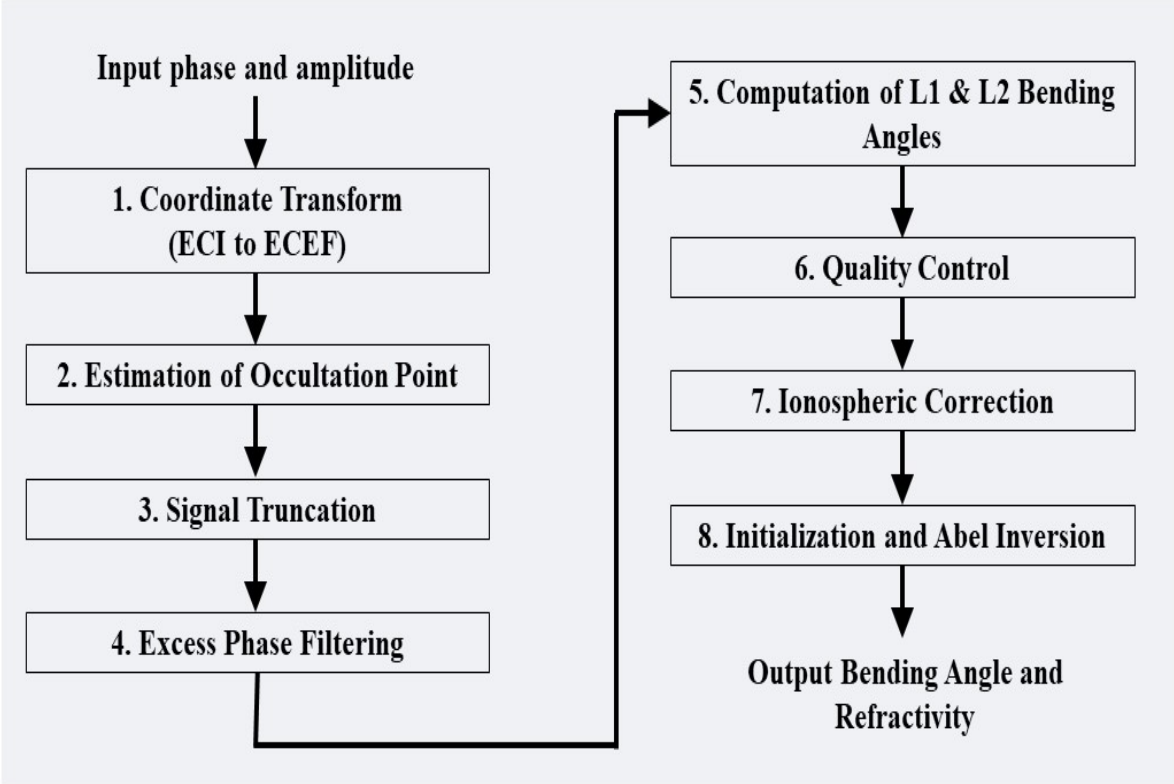

Figure 7. Flow chart depicting the different steps used in the NOAA STAR inversion of geometry and phase data to bending angle and refractivity profiles.

Table 1. Overview of the implementation of the STAR processing chain

Processing Step	Implementation Method
Input data	UCAR orbit in Cartesian ECI coordinates, L1 and L2 excess phase and SNR data
Coordinate Transform	ECI coordinates to ECEF Coordinate transform
Signal Truncation	Based on L1 SNR; use threshold on calculated base SNR
Excess Phase Filtering	Fourier Filtering using 0.5 second window on L1 and L2 excess phases
Bending Angle Computation	Full Spectrum Inversion
Quality Control	Mean L1 – L2 difference at 25 – 50 km < 100 μrad
Ionospheric Correction	Linear combination of L1 and L2 bending angles
Initialization	Exponential fit above 40 km
Refractivity Calculation	Abel inversion of the ionospheric corrected bending angle with the exponential fit

3.1.1 Data Inputs

The input data to the inversion system includes CDAAC provided Level L1b data that includes time series of GNSS and LEO satellite positions and velocities in ECI coordinate systems, and excess phase and SNR in L1 and L2 bands. The excess phases have navigation data modulation (NDM) removed, so unlike the COSMIC data, the current COSMIC-2 excess phase data does not require NDM removal in the excess phase pre-processing. Table 1 shows the implementation schemes of the STAR processing chain.

3.1.2 Convert L1 data from Cartesian Earth-centered Inertial (ECI) Coordinate to Earth-center Earth-Fixed (ECEF) Coordinate

UCAR Level L1b geometry data are provided in Cartesian Earth-centered Inertial (ECI) coordinate system. The first part of the processing involves conversion of the ECI coordinate system to Earth-center Earth-Fixed (ECEF) coordinate system. This step is required so that the position of the tangent points can be calculated at each time stamp to determine the representative occultation point for each profile.

3.1.3 Transform the Reference Frame to the Local Center of Earth's Curvature

The inversion of excess phase to bending angle is based on the assumption of the spherically symmetric atmosphere. In order to satisfy the spherically symmetric atmosphere approximation, the inversion of the phase data needs to be performed relative to local spherical symmetry tangential to the earth's ellipsoid. In all the RO measurements, the tangent points drift with altitude, so a representative reference position needs to be determined to assign to each RO measurement. In the

STAR processing, the center of curvature is determined at the point where the straight-line tangent point intersects the earth's ellipsoid.

3.1.4 Determine the Signal Truncation Point

The next step is to determine the signal truncation point, which is the point where the signal is stronger than the noise, so that the noise cab be effectively removed from the useful data. Signal truncation is dynamically determined for each occultation event based on the calculated base SNR. The base SNR represents the SNR value at which the noise becomes dominant and the useful signal cannot be distinguished from the noise. This step is important because the inversion from phase to bending angle uses the Fast Fourier Transform of the complete occultation signal and inclusion of the noise deteriorates the quality of the inverted signal. However, there is a trade-off in the selection of the truncation point of the signal. Truncating the signal very high results in loss of the higher bending angle components causing negative bias in the retrieved bending angle, and a decrease in the penetration depth. A lower truncation point may introduce noise.

In the NOAA STAR processing the truncation point is determined in two steps. The base SNR is determined for each time series using the lowest 5-seconds of the data smoothed using a 1-second moving average. Starting from the lowest tangent point of the time series, first a point is determined where the SNR is 3 times the base SNR. Once the first point is established, the final cutoff point is determined by going backwards towards lower tangent points at the point where the SNR first drops below 2 times the base SNR. These thresholds are subjective, but are selected so that small SNR jumps observed at low levels in the tropical RO observations are excluded in the processed profile.

Figure 8 shows an example of the truncation of the signal for RO sounding taken on October 01, 2019. The original signal is shown in grey, and the truncated signal in black. Figure 2 (a) shows the SNR and Fig. 2 (b) shows the excess phase (grey/black) and Doppler (blue/red) of the original/truncated signal. The figure illustrates that the SNR after 78 seconds reaches a base value. The excess Doppler shows that the significantly larger Doppler variations after the truncation point.

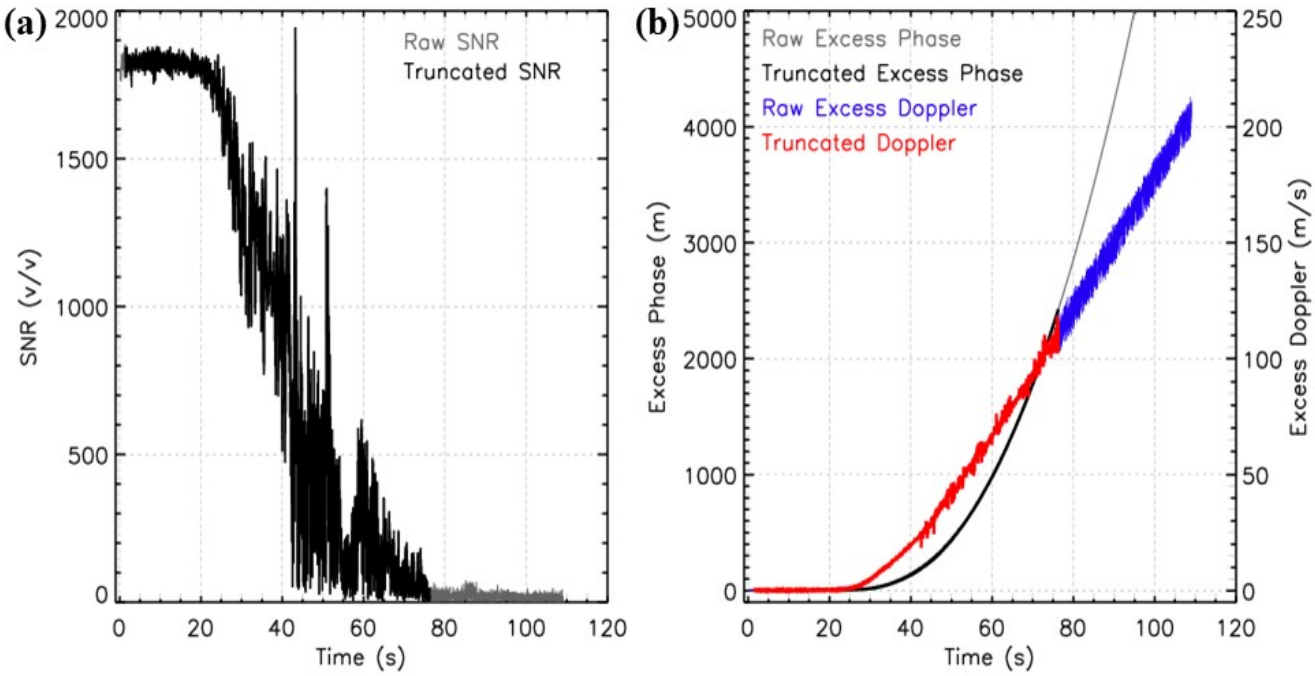

Figure 8. An example of the signal truncation scheme used in NOAA STAR processing, (a) SNR of the original/truncated signal in grey/black, and (b) excess phase of the original/truncated signal in grey/black and original/truncated Doppler in blue/red.

3.1.5 Noise Filtering of the Excess Phase

The RO signals are known to be affected by noise that affects the retrieved bending angles. The effect of noise can be reduced by applying low-pass filter. In the current version of the inversion, Fourier filtering is done on the observed excess phase with a window of 0.5 seconds. **Figure 9** shows the Doppler for the raw signal and the smoothed signal for the RO measurement shown in **Fig. 8**.

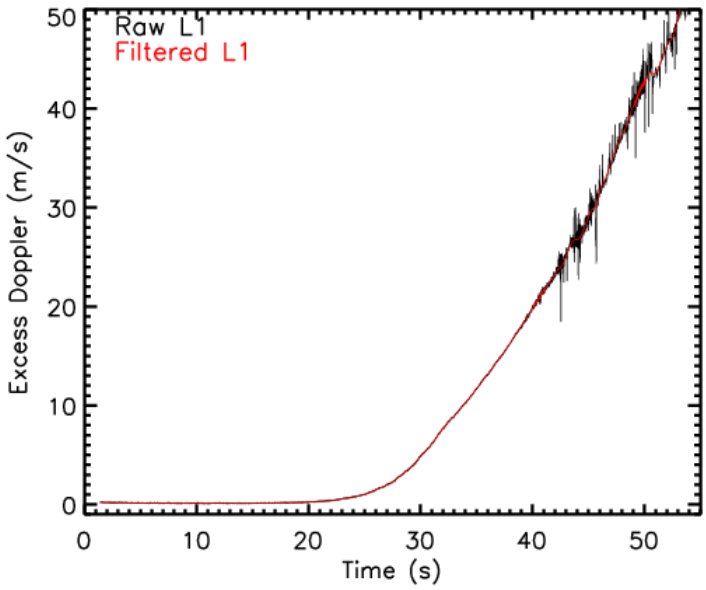

Figure 9. Excess Doppler for the RO sounding on October 01, 2019.

3.1.6 Inversion of phase to determine L1 and L2 bending angles

The inversion of the truncated signal uses the Full Spectrum Inversion (FSI). The FSI method is one of the several wave optics methods that can determine the different frequency components of the signal in the presence of multipath. It is based on the assumption that the Fourier transform of the entire signal can be computed using the method of stationary phase. They demonstrated that for a uniformly circular orbital geometry, the derivative of the phase of the Fourier transform with respect to frequency gives the central angle formed by the radius vectors to LEO and the GNSS, and the total frequency of each ray is proportional to the impact parameter. The impact parameter and the central angle can be used with radius vectors to calculate the bending angle at each of the impact parameter values.

In the inversion of the RO signal, it is customary to use geometric optics (GO) that assumes monotone signal received at the receiver, in the upper atmosphere where this assumption is valid and then use Fourier operator based wave optics (WO) in the lower atmosphere and then combine these separate methods into a single profile. The vertical spacing of the GO inversion is determined by the sampling frequency, whereas the WO methods the vertical sampling is independent of the signal sampling rate. This can cause a noticeable discontinuity in the retrieved bending angle profile when the two separate inversion results are sewed together to get a single inversion. To avoid this discontinuity, the NOAA STAR inversion uses a single FSI inversion for the whole profile.

The bending angle profile inverted using the FSI method provides impact parameter and bending angle pairs for infinite range of values for the impact parameter, so it is important to determine the position of the lowest impact parameter and bending angle pair. Current inversion of the STAR inversion uses the amplitude of the Fourier transform to determine the lowest impact parameter, bending angle pair. First the amplitude is normalized by the amplitude of the mean amplitude of the signal between 10 and 50 km. The lowest point is then determined where the amplitude is < 0.5 of

the normalized amplitude. **Figure 10** shows the determination of the lowest impact parameter and the corresponding bending angle. **Figure 10 (a)** shows the raw bending angle profile in blue and the cutoff profile in red. **Figure 10(b)** shows the normalized amplitude of the Fourier transform and the cutoff impact parameter. The figure illustrates the importance of the cutoff because the bending angle below the cutoff impact height (shown as blue curve in **Fig. 10 (a)**) is purely noise.

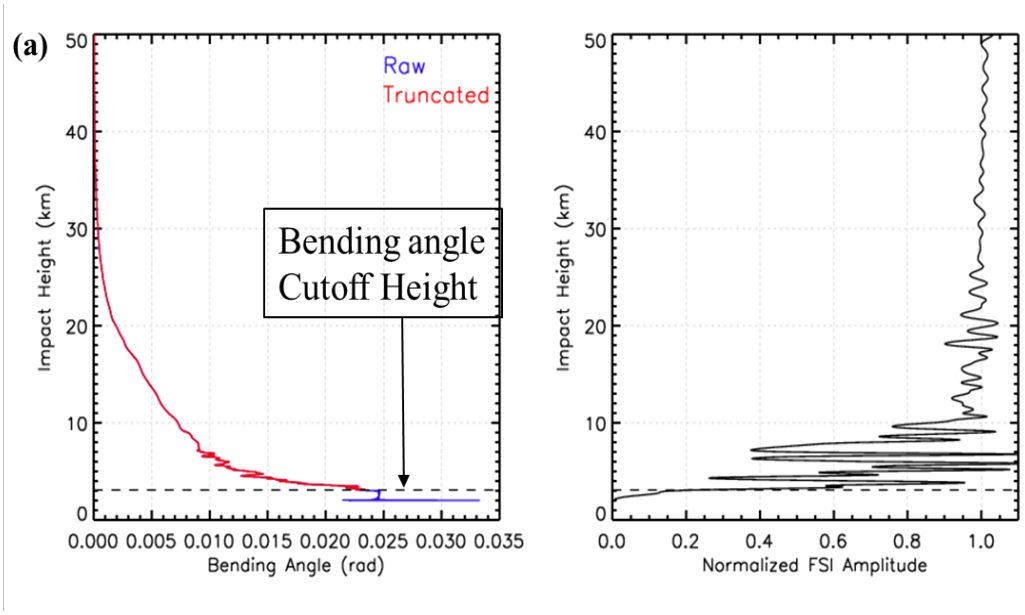

Figure 10. Illustration of the impact parameter cutoff point in the FSI Inversion method.

3.1.7 Quality control on the inverted bending angles

Bending angles are inverted separately for L1 and L2 bands, and smoothed using a sliding window of 125-m. Using the retrieval from the L2 band, bad profiles are determined using the lowest L2 impact height. All the profiles with lowest L2 impact heights > 20 km are discarded. Currently, 20 km height is used as the transition above which linear combination is applied for ionospheric corrections, so all the profiles with minimum L2 impact height > 20 km are discarded. The bending angle quality is determined using the difference of the mean L2 – L1 bending angle at 35 – 50 km impact height. RO profiles with the mean bending angle difference > 10 μrad are flagged as 'bad' profiles. This flagging was done to flag profiles with noisy L1 and/or L2 excess phases.

3.1.8 Ionosphere Correction of L1 Bending Angle

The ionospheric corrected bending angle (α_c) is calculated using two different approaches for impact heights above and below 20 km. For impact heights above 20 km, α_c is calculated as a linear combination of L1 (α_{L1}) and optimally smoothed difference of L1 and L2 bending angles ($\alpha_4 = \alpha_{L1} - \alpha_{L2}$)

$$\alpha_c = \langle \alpha_{L1} \rangle_{w1} + \frac{f_1^2}{f_1^2 - f_2^2} \langle \alpha_4 \rangle_{w2}. \quad (1)$$

The *w1* and *w2* represent the smoothing window used for α_1 and α_4, respectively. The w1 is fixed at 0.5 km, and the w2 is determined dynamically. For impact height < 20 km, the mean of the difference of L1 and L2 bending angles at impact heights 20 – 23 km is added to the L1 bending angle.

3.1.9 Calculation of Refractivity Using Abel Integration

Abel integration is then used on the ionospheric corrected bending angle to calculate the refractivity profile as a function of geometric altitude. For the refractivity calculations, the bending angle profiles up to 40 km are used, and the bending angle above 40 km height are approximated by exponential function with a scale height of 7 km.

3.2 Comparison with UCAR products

The UCAR bending angles and refractivity profiles from August 28 – September 13 are compared with corresponding STAR bending angle and refractivity profiles and simulated bending angle and refractivity from ERA5 data. **Figure 11(a) and 11(b)** show the mean and standard deviation of the fractional difference between the UCAR – ERA5 bending angle and refractivities, respectively. Similarly, **Fig. 11(c) and 11(d)** show the fractional difference of UCAR – STAR bending angle and refractivity, respectively.

The profiles show very consistent mean values above 8 km, with mean difference < 0.1 % and standard deviation of 3.15 and 1.12 % for bending angle and refractivities, respectively for the fractional difference of the UCAR – ERA5 quantities. The corresponding standard deviation of the fractional difference between UCAR and STAR are 2.5 and 1.5 %, respectively. The number of profiles used in the comparison is shown in green. UCAR bending angle and refractivity shows a negative bias in the lowest 3 km relative to both the ERA5 and STAR. The bending angle comparison with STAR shows a positive bias in the 4 – 8 km range, and a positive bias above 30 km. The small scale fluctuations in the 15 – 20 km can be expected because of the differences in the vertical resolutions of reanalysis data and RO data near the tropopause.

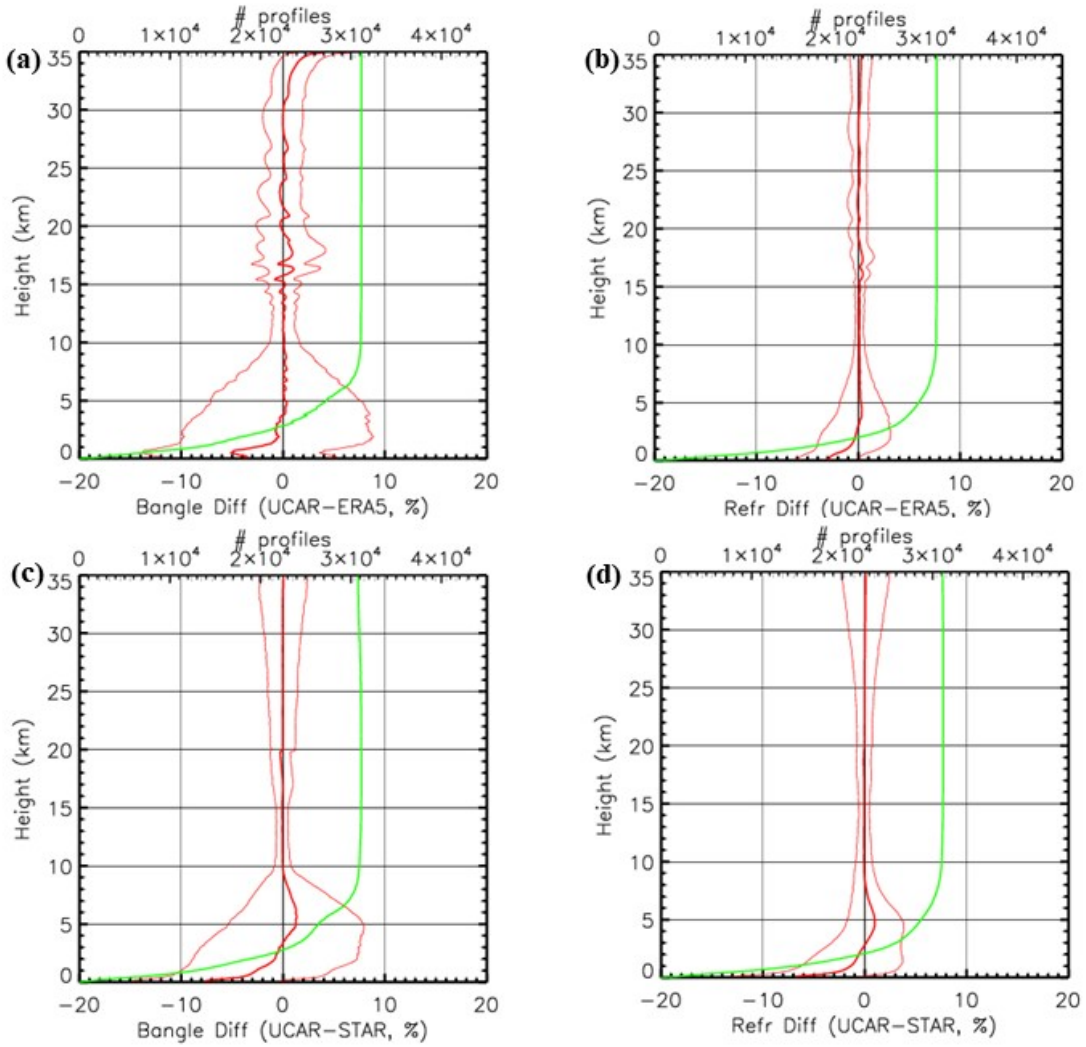

Figure 11. Fractional differences of UCAR – ERA5 (a) bending angles and (b) refractivity and UCAR – STAR (c) bending angle, and (d) refractivity for data from August 28 – September 2019. The thick red line represents the mean and the thin lines represent 1 standard deviation from the mean. Green curves show the number of profiles used for the comparison.

Figure 12 show the latitudinal distribution of the fractional bending angle (**Fig. 12(a)**) and refractivity (**Fig. 12(b)**). **Figure 12 (c) and 12 (d)** show the fractional difference of the bending angle and refractivity, respectively, at different SNR values. The red curves represent the mean and one standard deviation from the mean, and the green curve shows the number of profiles used in each bin. The fractional difference in the bending angle and refractivity profiles show smaller standard deviations in the southern hemisphere sub-tropics compared to the other latitude bands. One of the factors contributing to the variance in the bending angles and refractivity are the amount of water vapor in the atmosphere. Since the data used consists of mostly northern hemisphere summer and fall seasons, the southern hemisphere mid-latitude variations are expected to be smaller than at other latitude bands.

COSMIC-2 SNR in L1 band shows large variation in the range 300 – 2600 v/v. Larger SNR is not expected to significantly improve the quality of the data at altitudes above 10 km, which is illustrated by the similar mean and standard deviation characteristics of fractional differences of both bending angle and refractivities. At altitudes below 5 km, mean shows a slightly larger negative bias in comparison with ERA5 for those observations with SNR < 500 v/v.

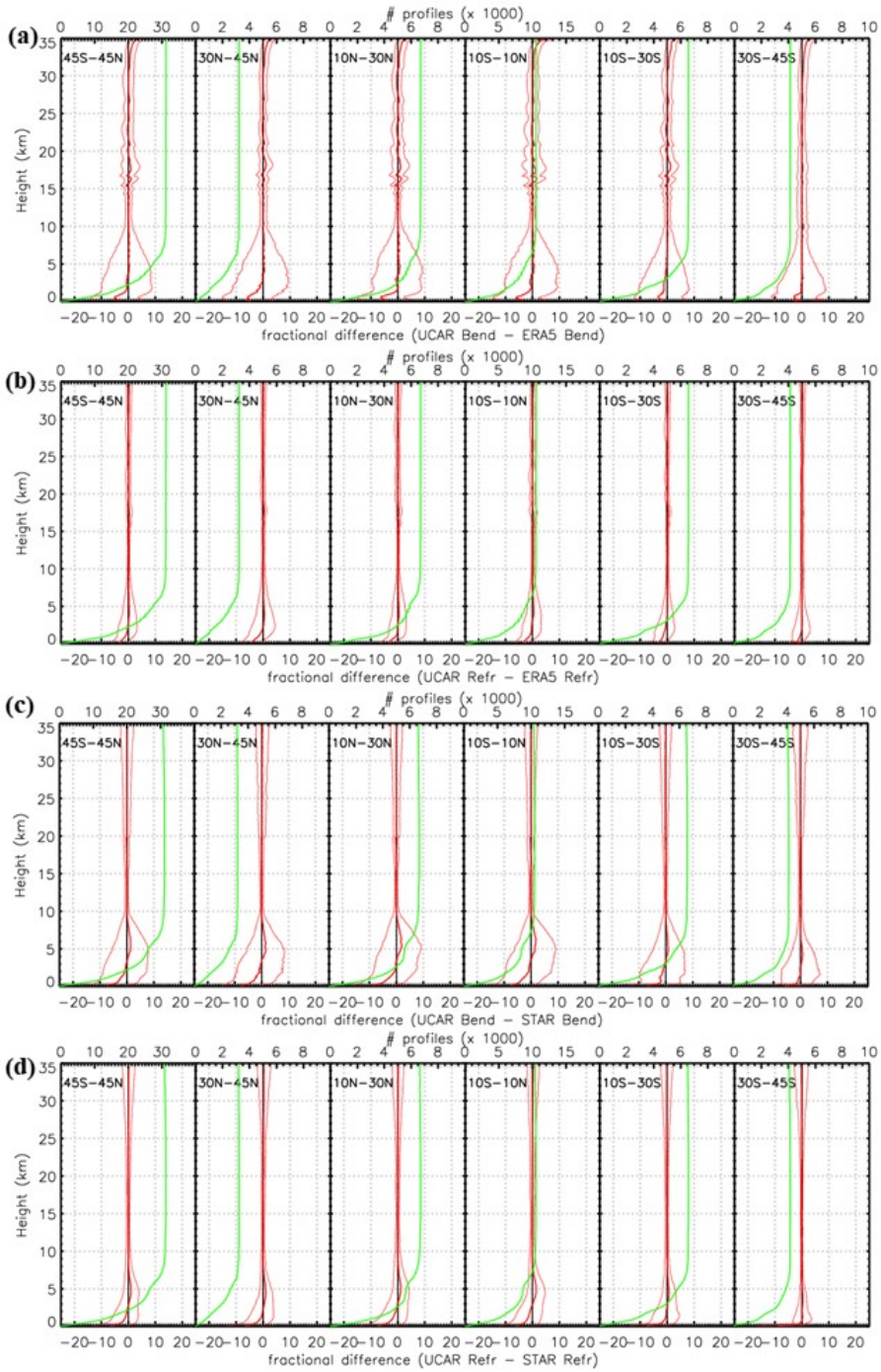

Figure 12. Latitudinal distribution of the UCAR – ERA5 (a) fractional bending angle, (b) fractional refractivity, and UCAR – STAR (c) fractional bending angle, (d) fractional refractivity differences. The number of profiles used in each latitudinal bin is shown in green.

4. Development of STAR 1D-var Algorithm to Derive Temperature and Moisture Profiles in the Neutral Atmosphere

Temperature and water vapor play a crucial role in weather and climate. Accurate global water vapor and temperature estimates, particularly in the middle and lower troposphere (LT), are extremely important for understanding the physics of convective cloud systems, precipitation, the hydrological cycle, and the energy balance of the Earth. In this section, we describe the STAR 1D-var inversion algorithm that inverses RO refractivity profiles into temperature and moisture profiles in the neutral atmosphere.

4.1 STAR 1D-var Inversion Approaches

The 1D-var methodology is to retrieve temperature $T(P)$ and water vapor partial pressure $P_W(P)$ from observed refractivity $N(P) = 10^6 \times (n(P) - 1)$ at atmospheric pressure level P using optimal estimation technique (Rodgers, 2000). Retrieved variables (temperature and water vapor) in each vertical level are processed independently, thus "measurement vector" is degraded to scalar value for RO 1D-var algorithm, and "retrieved vector" consists of two elements, i. e. temperature and water vapor on each level.

One radio occultation event provides vertical profile of atmospheric refractivity, from which profiles of atmospheric constituents $T(P)$ and $P_W(P)$ are retrieved in corresponding altitude range. Refractivity N is related to the atmospheric temperature T and water vapor partial pressure P_W at the perigee of line of sight with pressure P by the following equation:

$$N = FM(T, P_W) = 77.6\frac{P}{T} + 3.73 \times 10^5 \frac{P_W}{T^2} \quad (1)$$

Here P, T, and P_W are in mbar, Kelvin, and mbar units respectively, and FM means RO Forward Model. For given measurement Y_{OBS}, the optimal estimation of retrieval vector $X = (T, P_W)$ is derived from the following iterations:

$$X_{i+1} = X_0 + (K_i^T E^{-1} K_i + B^{-1})^{-1} \times K_i^T E^{-1}\{(Y_{OBS} - Y(X_i)) + K_i(X_i - X_0)\}, \quad (2)$$

where $\boldsymbol{X_0} = (T_0, P_{W_0})$ is the first guess, $\boldsymbol{K} = \left(\frac{\partial N}{\partial T}, \frac{\partial N}{\partial P_W}\right)$ is Jacobian vector, $\boldsymbol{B}$ is a priori background covariance matrix, and $\boldsymbol{E}$ represents instrument noise and the forward model error covariance matrix. The index $\boldsymbol{i}$ corresponds to iteration number. Iterations are continued until residual between observed refractivity N_{OBS} and simulated one from retrieved state $N_i = FM(T_i, P_{W_i})$ satisfies to the condition $|N_{OBS} - N_i|/N_{OBS} \leq 0.001$ (0.1 %). The retrieval is considered to be successful when two conditions are met: 1) iterations are converged, i. e. N-residual has reached the threshold value; and 2) retrieved water vapor partial pressure P_{W_i} is positive.

To take into account of seasonal and spatial variability of the Earth's atmosphere, background atmospheric covariance matrix $\boldsymbol{B}$ and measurement noise matrix $\boldsymbol{E}$ have been evaluated separately for five latitude zones (North Polar 90N to 60N, North Mid-Latitudes 60N to 20N, tropics 20N to 20S, South Mid-Latitudes 20S to 60S, and South Polar 60S to 90S) and by monthly averaging.

NOAA/NCEP Global Forecasting System (GFS) data have been used to evaluate background state covariance matrix $\boldsymbol{B}(\boldsymbol{Lat}, \boldsymbol{Mon})$. Averaging has been done separately for each month and each of five latitude zones. Thus, 60 total estimates of background states have been computed by means of mean profiles and standard deviation for atmospheric temperature and water vapor. Then diagonal elements of covariance matrix $\boldsymbol{B}$ are set to be equal to the square of corresponding standard deviation, while off-diagonal elements are set to zeros.

The same set of GFS background states has been used to derive simulated refractivity N, using RO forward model. Then measurement noise matrix $\boldsymbol{E}(\boldsymbol{Lat}, \boldsymbol{Mon})$ was defined as a matrix with off-diagonal elements equal to zero and diagonal elements proportional to the variance of N, on monthly basis and separately for each latitude zone:

$$\boldsymbol{E_{ij}} = \{\boldsymbol{\gamma_{Noise}} \times \boldsymbol{\sigma}(\boldsymbol{N_i})\}^{\boldsymbol{2}}, \qquad \boldsymbol{i = j}$$

$$\boldsymbol{E_{ij}} = \boldsymbol{0}, \qquad \boldsymbol{i \neq j}$$

Low values of γ_{Noise} lead to instability of inversion, i.e. less number of successful retrievals. On other hand, high values of γ_{Noise} result in loosing of measurement information content, and retrievals would be closely tight to first guess state. After trials, it was found that $\gamma_{Noise} = 0.1$ is optimal value in trade-in between these two factors. For this value of γ_{Noise}, the measurement noise is about 1% of expected observed refractivity. Finally, first guess profiles to initiate retrieval iteration are taken from GFS Forecast data within 3-6 hours and 1-degree of latitude/longitude from time and location of RO observations.

STAR RO 1D-Var retrieval algorithm has been intensively validated on COSMIC and COSMIC-2 data that proved its workability and robustness, before applying it for COSMIC-2 analysis. Detail validation analyses of the STAR 1D-var retrievals are not shown in this report.

4.2 Comparison with UCAR retrievals

At the first stage, we have compared STAR 1D-var retrievals of water vapor with water vapor, obtained at UCAR processing center, which we considered as a "Truth". This comparison was done with COSMIC-1 data over the year of 2018 and presented on **Figure 13**. Blue lines present statistics (bias and bias$\pm$rmsd) for FG-UCAR, and red lines are for STAR-UCAR. The difference between blue and red lines generally show how much job was done by retrieval to correct first guess. One can see that STAR retrievals tend to UCAR ones, compensating bias with first guess and making rmsd 2-3 times less over altitude range 0-12 km. This is especially noticeable in tropics, where RO measurements have high sensitivity to water vapor, and initial bias of more than 1 g/kg near the surface is gone to almost zero after retrieval, and rms decreases

from 1 g/kg to 0.5 g/kg. It should be noted that the purpose of this test was rather to prove that STAR retrievals do not contradict to UCAR ones, than to show the difference with actual atmospheric state. We left the latter one to independent comparison with RAOB observations what discussed under.

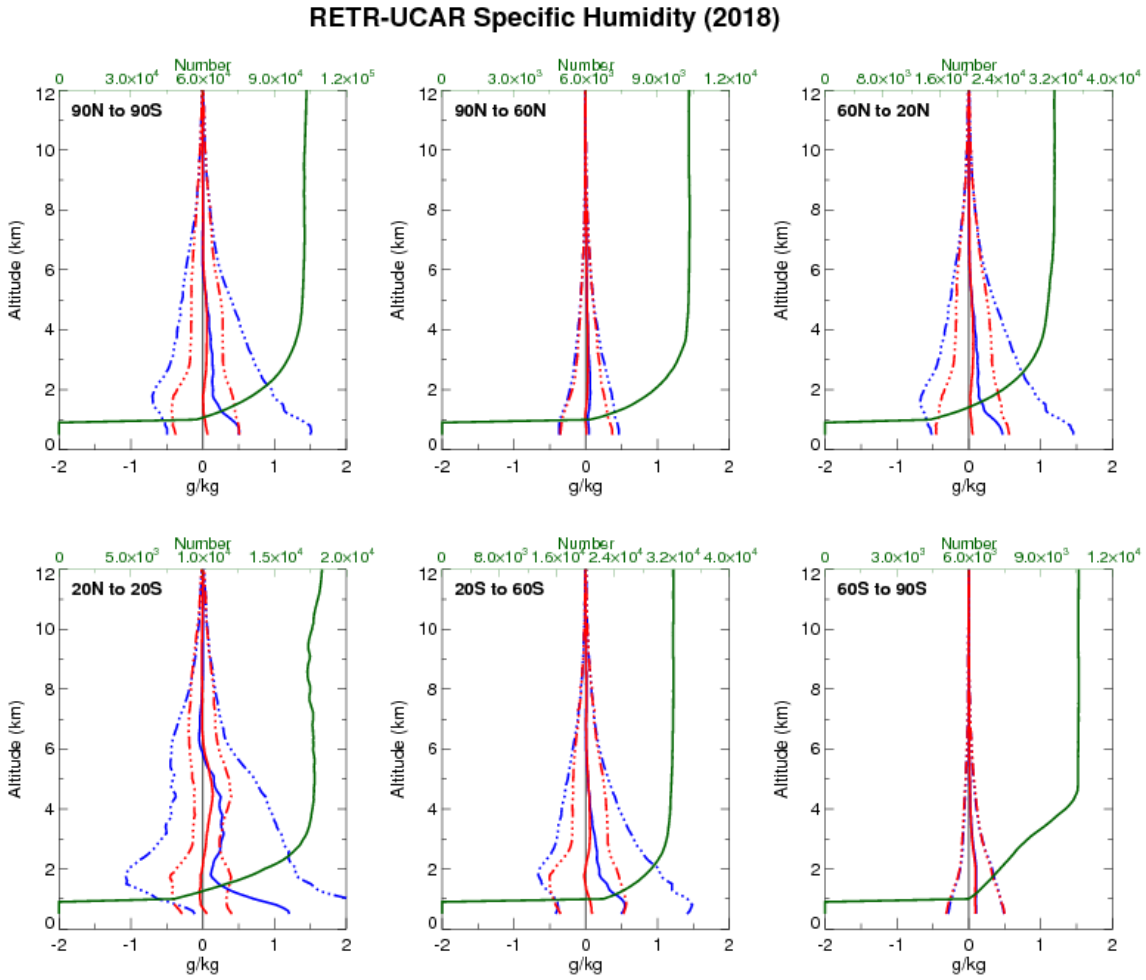

Fig. 13. Comparison of NOAA STAR RO retrievals with UCAR retrievals for specific humidity, average of 2018 for COSMIC-1 data. Blue lines: bias (solid line) and bias ± rmsd (dash-dotted lines) for First Guess - UCAR. Red lines: bias (solid line) and bias ± rmsd (dash-dotted lines) for RETR –UCAR. Green line is a sample size for each latitude zone.

5. STAR ICVS Tool Development

NOAA/NESDIS/STAR plays an important role in the Commercial Weather Data Pilot (COSMIC-2) studies. A STAR testbed center was established to routinely process the COSMIC-2 data. An Integrated calibration and validation system (ICVS) was also developed to routinely monitor the quality of the derived RO data.

A STAR operational inversion package was developed to process COSMIC, Metop-C, and COSMIC-2 2 data. COSMIC-2 R2 data were obtained from both GeoOptics and Spire Global. An interface page of the STAR GNSS RO ICVS is shown in **Fig. 14**.

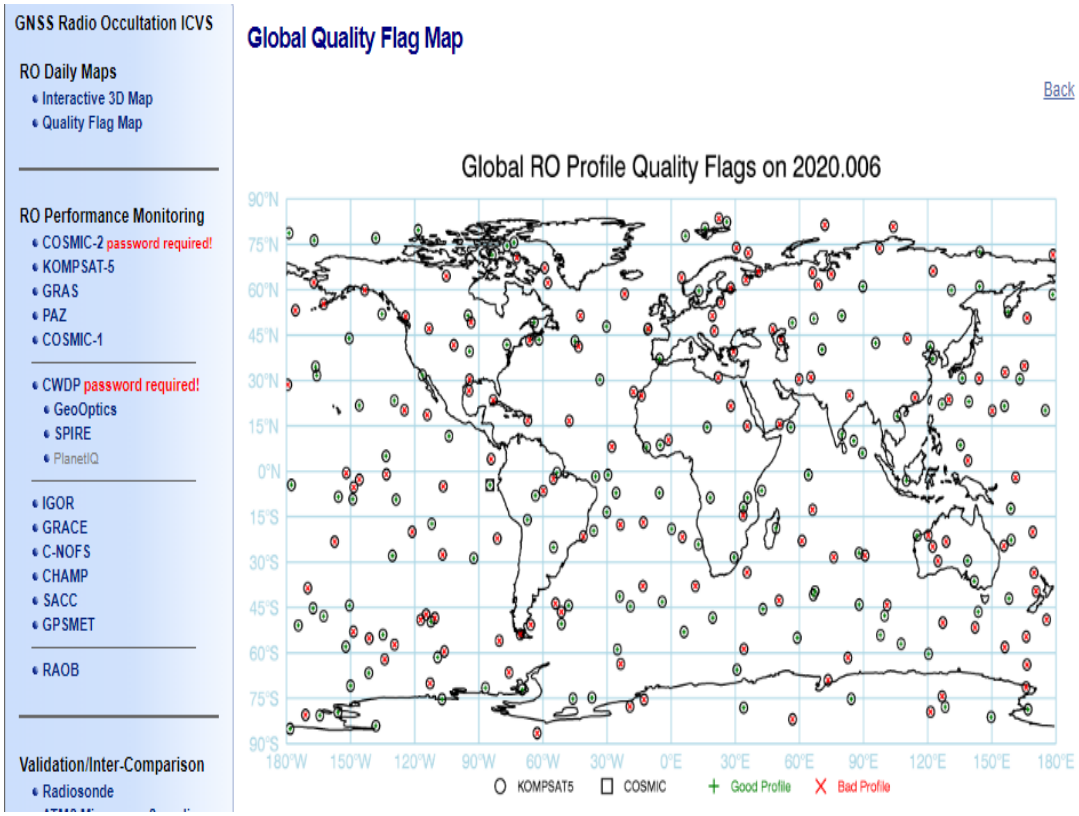

Figure 14. An interface page of the STAR GNSS RO ICVS.

STAR RO ICVS system can be seen under
https://ncc.nesdis.noaa.gov/GNSSRO/ICVS/index.php

The references used in the RO ICVS include weather model outputs, reanalysis, data from various RO missions, and radiosonde measurements. The functions of the STAR GNSS RO ICVS include:

- Near real time and long-term instrument status, performance monitoring, and anomaly diagnosis

- Near real time and long-term level 1 data product quality monitoring
- Provide real time support for sensor calibration activities
- Provide rapid and preliminary estimate of satellite data impact in NWP applications
- Ensure the integrity of the climate data records from all satellite instruments
- Currently, RO data from 12 publicly available missions are included, from GPSMET collected in 1995 to COSMIC2 data in 2019.
- RO data producer: UCAR, ROMSAF, ROPP and STAR (under testing). Monitoring RO product parameters and instrument performance at all levels.
- Routine comparison of atmospheric profiles with other satellite observations and retrievals including microwave, and infrared.
- Routine comparison of profiles with those from Radiosondes.
- Dynamic web interface with many capabilities.
- Long-term monitoring of the parameters.

6. Development of Multi-Sensor Validation System

In STAR we also work with in-house experts on IR/MW satellite data and in situ RAOB measurements to validate the accuracy and retrieval uncertainty of COSMIC-2 (and data from other RO missions). We also use measurements from other RO missions to validate the quality of COSMIC-2 data processed by UCAR.

6.1 Hyperspectral Infrared Sounder Data

High spectral resolution radiance data obtained from the Cross-track Infrared Sounder (CrIS) instrument are used to compare to the brightness temperatures converted from COSMIC-2 (and GeoOPTICS and SPIRE) temperature and water vapor profiles.

CrIS is a Fourier transform spectrometer. CrIS is the first in a series of advanced operational sounders that provide more accurate, detailed atmospheric temperature and moisture observations for weather and climate applications. It is the key instrument currently flying on the Suomi NPP and NOAA-20 satellites, and represents a significant enhancement over NOAA's legacy infrared sounder—the High Resolution Infrared Radiation Sounders (HIRS). CrIS provides soundings of the atmosphere with 2211 spectral channels, over three wavelength ranges: LWIR (9.14-15.38 μm), MWIR (5.71-8.26 μm) and SWIR (3.92-4.64 μm). The CrIS scans a 2200km swath width (+/- 50 degrees), with 30 Earth-scene views. Each field consists of nine fields of view which are organized as 3x3 array of 14km diameter spots (nadir spatial resolution).

Fig. 15 shows the peak weighting function location of CrIS LWIR (9.14-15.38 μm) channel, whose corresponding pressure levels range from ~0.1 to ~1000 hPa. In this study, the LWIR band channels will be used for comparison.

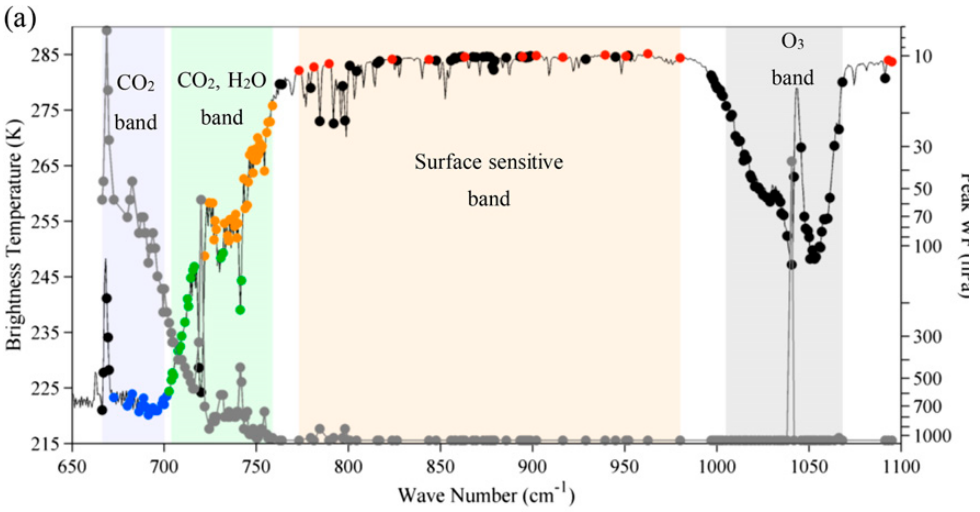

Figure 15. Peak weighting function pressure of the CrIS LWIR band vs. spectral wave-number together with brightness temperature observed over typical scene.

6.2 Microwave Sounder Data

The Advanced Technology Microwave Sounder (ATMS) is a cross-track scanner with 22 channels which provides sounding observations needed to retrieve profiles of atmospheric temperature and moisture for civilian operational weather forecasting as well as continuity of these measurements for climate monitoring purposes. Like the long heritage of its predecessors, ATMS combines all the channels of the preceding AMSU-A1, AMSU-A2, and AMSU-B sensors into a single package with considerable savings in mass, power, and volume. The ATMS covers 22 channels in bands from 23 GHz through 183 GHz. ATMS is currently onboard the NPP and NOAA-20, and will be on the follow-on JPSS missions.

Fig. 16 shows the weighting functions of ATMS channels. In this work, channels 6-15 of ATMS, whose peak sounding height ranges from 5 to 50 km, are used as reference to validate the RO temperature and/or humidity profiles.

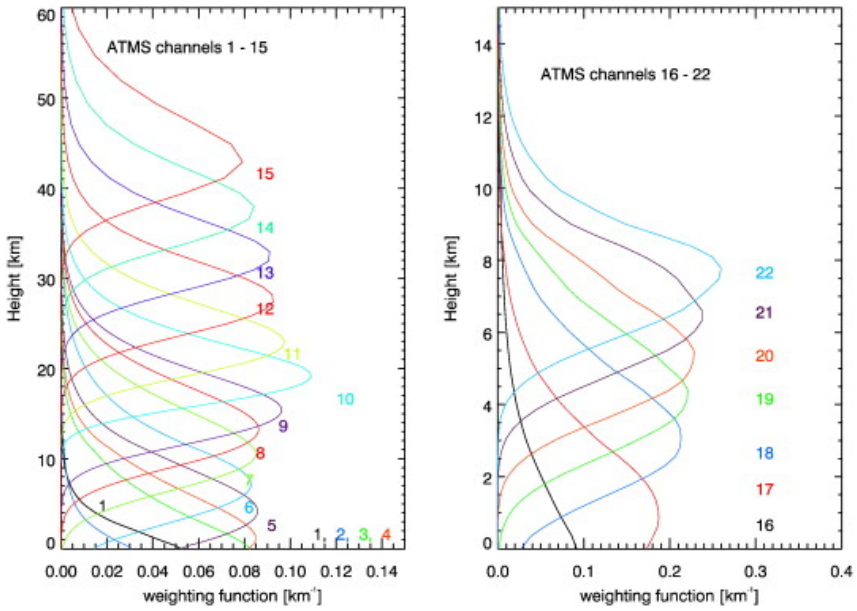

Figure 16. Weighting function of ATMS channels.

6.3 Radiative Transfer Model Simulations

This study makes use of the Community Radiative Transfer Model (CRTM) to convert the thermal profiles retrieved from RO observations to simulated brightness temperatures for direct comparison to satellite sounder observations. CRTM is a fast radiative transfer model for calculations of radiances for satellite infrared or microwave radiometers, and is able to output infrared/microwave radiance and brightness temperature at CrIS/ATMS's spectral resolutions.

The modeling bias analysis scheme enables evaluation of COSMIC-2 RO data bias at different pressure levels with respect to atmospheric reanalysis background data through comparison with the CRTM-modeled brightness temperature using the temperature from infrared and microwave sensors and global atmosphere reanalysis data from ECMWF.

Table 2 summarizes the setup of the simulation model for radiative transfer modeling (RTM). In the case of cross-instrument (IR/MW vs. RO) temperature bias evaluation, the temperature and humidity profile data retrieved from RO sensor measurements are used as input to the CRTM simulation. The CRTM-simulated BT from RO, e.g. COSMIC-2, GeoOptics, SPIRE and MetOp-A/B, measurements and observed BT by IR/MW sensors are compared for cross-instrument bias evaluation.

Table 2. Input Variables and Parameters for RTM Simulation with CRTM.

Category	Variable	Data source
Atmosphere	Level and layer pressure temperature	RO
	Specific humidity	ECMWF or RO
	Ozone mass mixing ratio	ECMWF
Surface	Water type	1 (sea water)
	Skin temperature	ECMWF
	Wind speed	ECMWF
	Wind direction	ECMWF
Geometry	Altitude	Satellite data
	Satellite zenith angle	Satellite data
	Satellite azimuth angle	Satellite data
	Solar zenith angle	Satellite data
	Solar azimuth angle	Satellite data
	Latitude/longitude	Satellite data
Parameters	Climatology	U.S. standard profile
	Water coverage	1 for ocean

Surface parameters including skin temperature, wind speed and wind direction are obtained from ECMWF's ERA-Interim reanalysis model which is based on 6 hourly increments (http://www.ecmwf.int/en/research/climate-reanalysis/era-interim). The 0.75° spatially gridded model level product has a resolution equivalent to ~80 km.

Ozone, water vapor, and temperature (used for O-B comparison) profiles are also obtained from ECMWF's ERA-Interim reanalysis pressure level data which are coordinated at 37 mandatory pressure levels and is available from ground to up to ~0.1 hPa.

In the RO vs. background/model data analysis, the matchup condition is set as restricting the co-location between RO sensor data and background/model data to be within 200 km distance difference and a 3-hour time difference.

6.4 Comparison Results

6.4.1 Comparison to other Radio Occultation Data

In this study, we used UCAR processed KOMPSAT-5, COSMIC, TSRX, Metop-A, and Metop-B are used to compare to those of collocated COSMIC-2 data. In addition. the early phase of the COSMIC-2 mission, when these six COSMIC-2 receivers were closely located, provided a unique opportunity to test the precision of GPS RO measurements, where the GPS RO signals travel through nearly the same atmospheric paths. The differences in refractivity between COSMIC RO soundings (when their tangent points are less than 10 km apart were compared to provide an estimate of the precision of the GPS RO technique. **Fig. 17** depicts the mean and standard deviation of the fractional difference for BA (**Fig. 17a**), fractional difference for refractivity (**Fig. 17b**), and temperature difference (**Fig. 17c**). The results show that the mean differences are equal to 0.01% with a std of 1.52 for fractional BA difference.

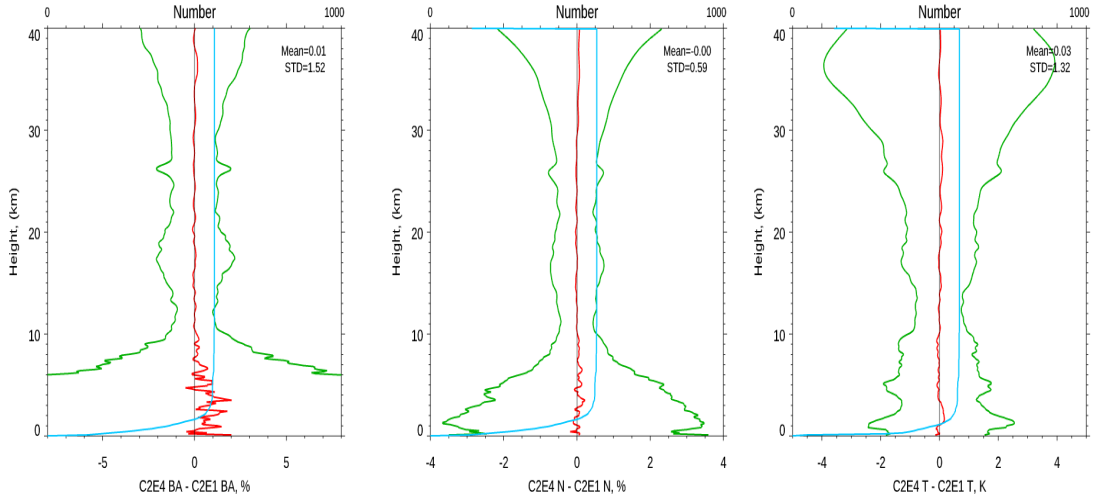

Figure 17. The mean and standard deviation of the fractional difference for BA (left panel), fractional difference for refractivity (middle panel), and temperature difference (right panel).

Fig. 18 depicts the fractional BA mean difference between COSMIC-2 and other collocated RO missions (COMSIC-1, KOMPSAT-5, TSRX, Metop-A, and Metop-B) at different vertical layers from Oct. 2019 to Jan. 2020.

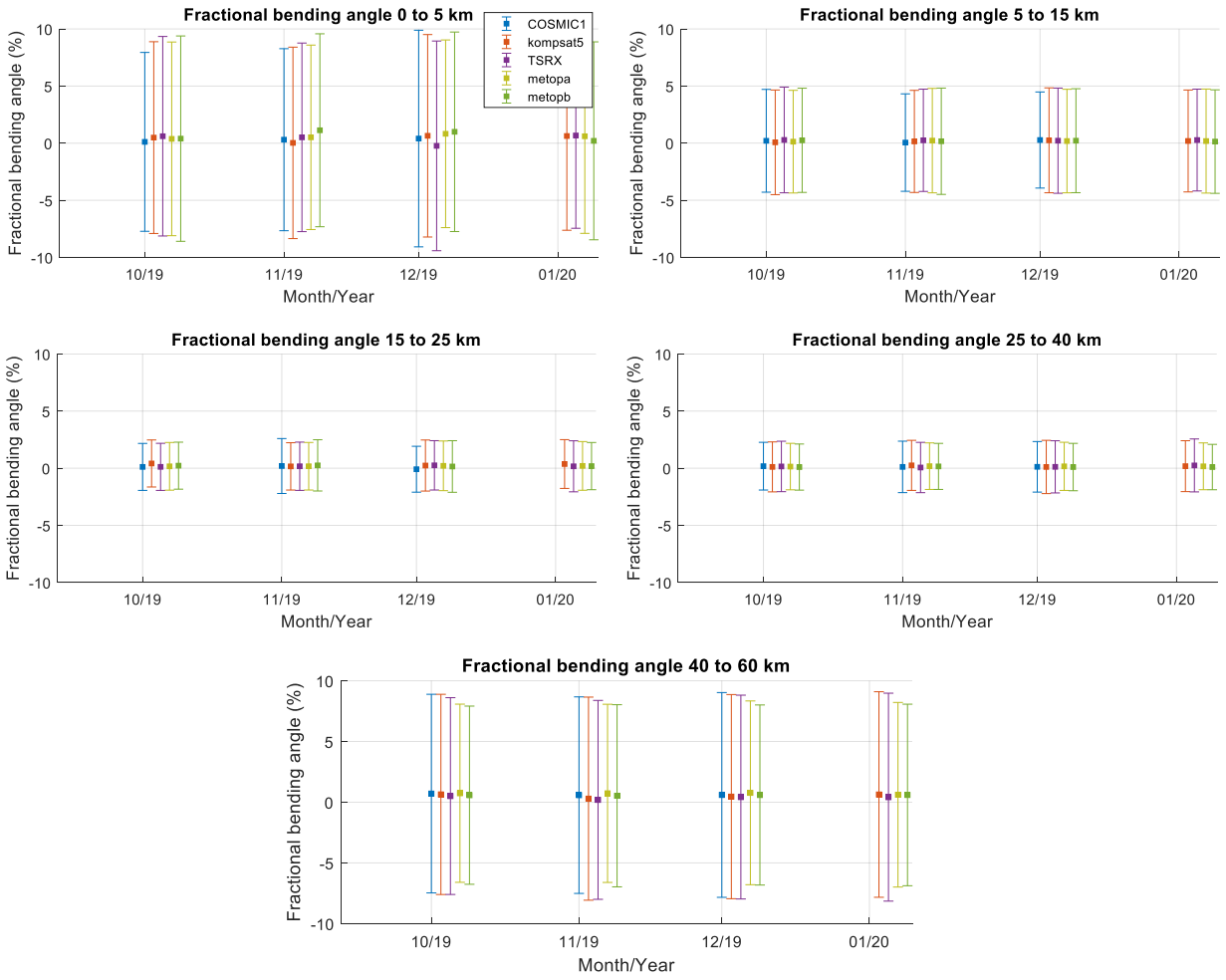

Figure 18. The fractional BA mean difference between COSMIC-2 and other collocated RO missions (COMSIC-1, KOMPSAT-5, TSRX, Metop-A, and Metop-B) at different vertical layers from Oct. 2019 to Jan. 2020.

6.4.2 Comparisons to CrIS data

The evaluation of multi-RO data quality is performed through comparison of CRTM-modeled BT from multi-RO data with the observed BT data by sounding IR instruments such as infrared sounder CrIS on NPP/NOAA-20. As can be identified from the weighting function peak location of CrIS channels, there exist spectral bands, e.g. LWIR (9.14-15.38 μm) channel and SWIR (3.92-4.64 μm), whose sounding pressure levels range from ~0.1 to ~1000 hPa. These bands will be used to evaluate the RO vs. IR profile bias at different pressure levels. Through double-difference of RO vs. IR BT bias, the multi-RO sensor bias will also be evaluated. The initial brightness BT differences are shown in **Fig. 19**. The double difference results are shown in **Fig. 20**.

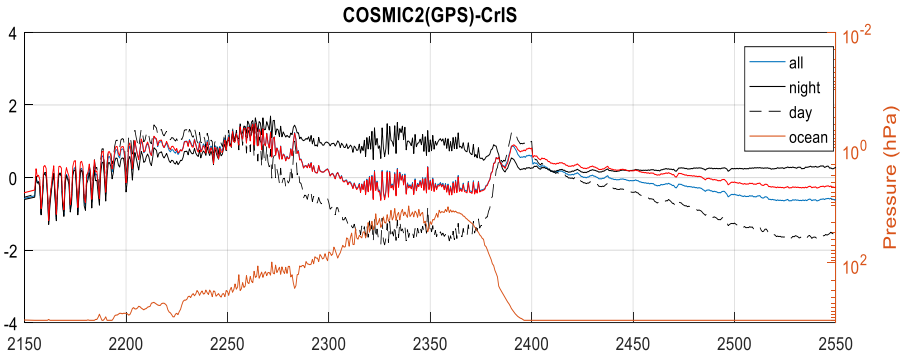

Figure 19. The COSMIC-2 (GPS) – CrIS when there are collocated within 200 km and 3 hours.

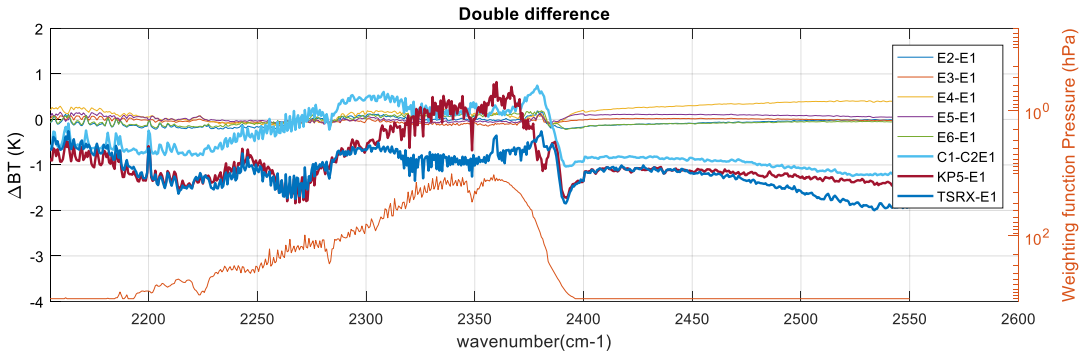

Figure 20. The double difference of to define RO-RO biases when CrIS are used as references.

6.4.3 Comparisons to MW data

The evaluation of multi-RO data quality is performed through inter-sensor comparison CRTM-modeled BT from multi-RO data with the observed BT data by ATMS on NPP and NOAA-20 are shown in **Fig. 21**. The weighting function peak locations of ATMS show that sounding channels #6-#15 of ATMS have peak sounding height ranges from 5 to 50 km and surface channels #19-#22 have peak height ranges from 3 to 7 km. These ATMS channel data will be used as reference to validate the RO temperature and humidity profiles at different height/pressure levels. Through double-difference of RO vs. MW BT bias, the multi-RO sensor bias will be evaluated. COSMIC-2 G refers to GPS datasets. COSMIC-2 R refers to GLONASS datasets.

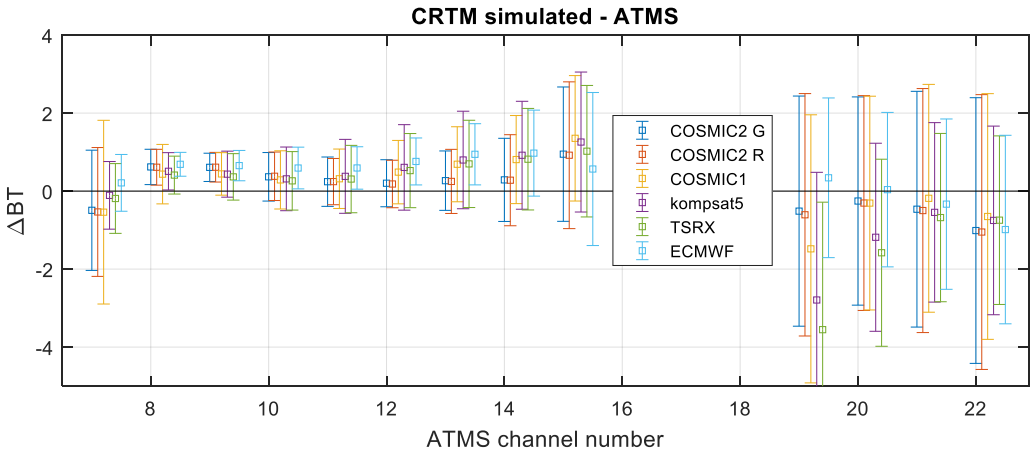

Figure 21. The evaluation of multi-RO data quality is performed through inter-sensor comparison CRTM-modeled BT from multi-RO data with the observed BT data by ATMS on NPP and NOAA-20.

7. Highlights of STAR RO Studies and Validation Results

The STAR processed COSMIC-2 retrievals are used to understand the quality of the RO raw phase delay data and to quantify the structural uncertainty of the derived bending angel profiles and refractivity profiles when different inversion methods and initialization approaches are implemented. The related COSMIC-2 tasks and their corresponding completion rate are:

- Participate in the COSMIC-2 "Neutral Atmosphere cal/val plan" (100% completion);
- Perform inter-comparisons of RO measurements among RO satellites and other sources (100% completion);
- Develop tools to support the COSMIC-2, KOMPSAT-5, PAZ and MetOP activities (85% completion);
- Perform Operational monitoring of RO instruments and derived data with the Integrated Calibration/Validation System (ICVS) (85% completion);
- Develop web interface for the ICVS monitoring to include identification of RO-derived data quality trending correlated with source, time and geolocation (90% completion);
- Develop bias monitoring regime including calculation of observed to model background (O-B) bias (90% completion);
- Perform RO observation impact assessments (working with JCSDA, AMOL, and EMC, 85% completion);

In this section we highlight the validation and application results performed during the period between April 2019 to April 2020.

7.1 Comparison between GeoOptics Bending Angle and STAR FSI Retrievals

STAR processing of the GeoOptics L1b data to bending and refractivity includes preprocessing of the L1 and L2 components that include (1) coordinate transformation from ECI to ECEF, (2)

determining local center of curvature and establishing new center of local curvature, (3) data truncation using dynamic SNR threshold, (4) applying FSI retrievals on L1 and L2 excess phases, (5) ionospheric correction and quality control on bending angles, and (5) inversion to refractivity using Abel inversion.

An inter-comparison of the bending angles from STAR, UCAR and JPL processing (for GeoOptics) shows stable STAR bending retrievals (**Fig. 22**). There is a positive bias in the STAR bending angle below 3 km relative to both UCAR and JPL bending angles.

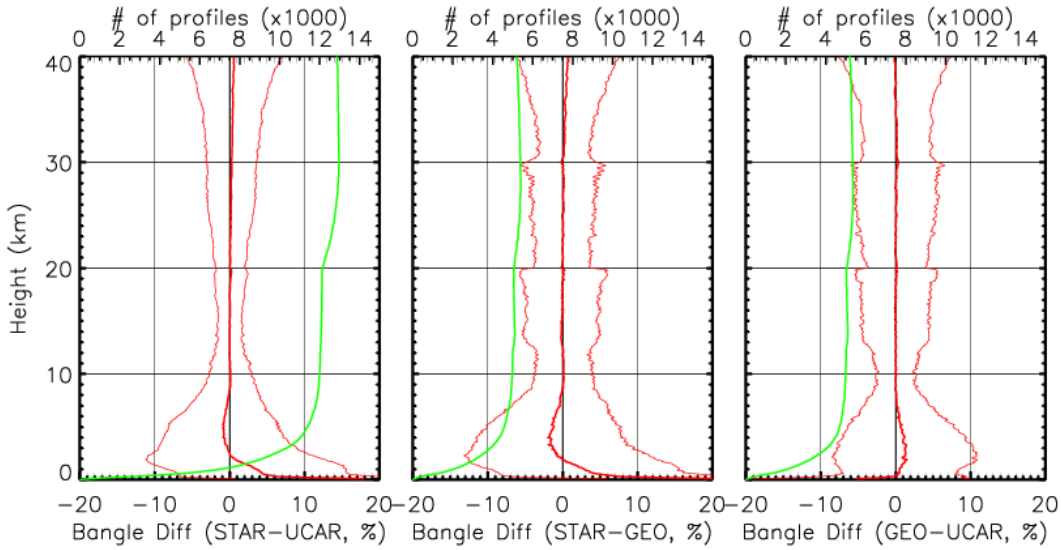

Fig. 22. Fractional bending angle differences for (left) STAR-UCAR, (center) STAR – JPL, and (right) JPL – UCAR.

7.2 Comparison between GeoOptics Refractivity and STAR FSI Retrievals

The refractivity obtained from the three processing centers also show similar biases to the bending angles (**Fig. 23**). The mean fractional refractivity differences are close to 0 from 6 km up to 35 km.

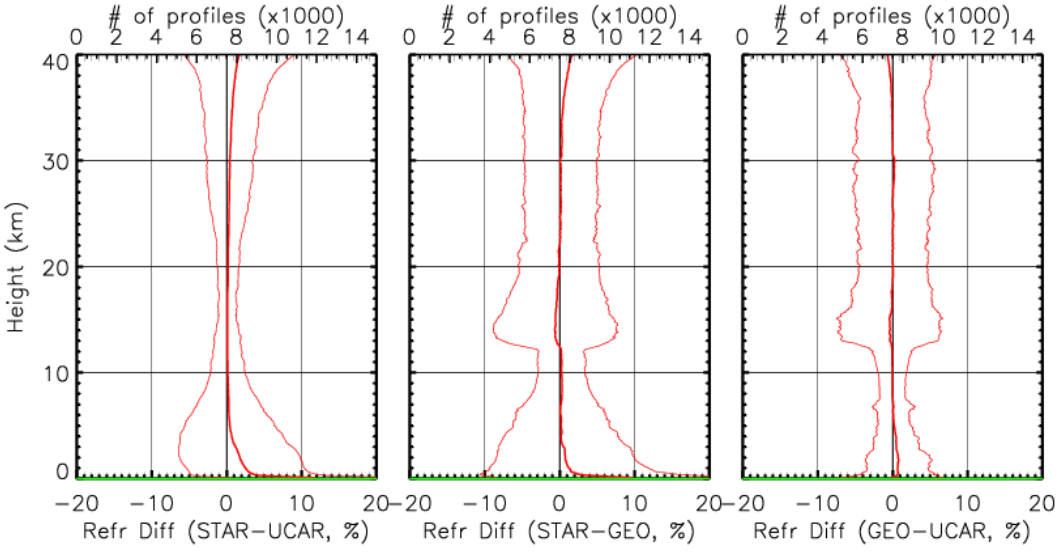

Fig. 23. Fractional refractivity differences for (left) STAR-UCAR, (center) STAR – JPL, and (right) JPL – UCAR.

7.3 Comparison between GeoOptics Data and STAR ROPP Retrievals

To quantify the general quality of GeoOptics bending angel, we compare multiple months of GeoOptics bending angel with those independently processed by ROPP where GeoOptics excess phases are used as inputs. **Figures 24a and b** depict the fractional bending angle difference and temperature difference between ROPP and GeoOptics. Results show that the GeoOptics bending angle profiles and temperature profiles are very close to those derived from ROPP.

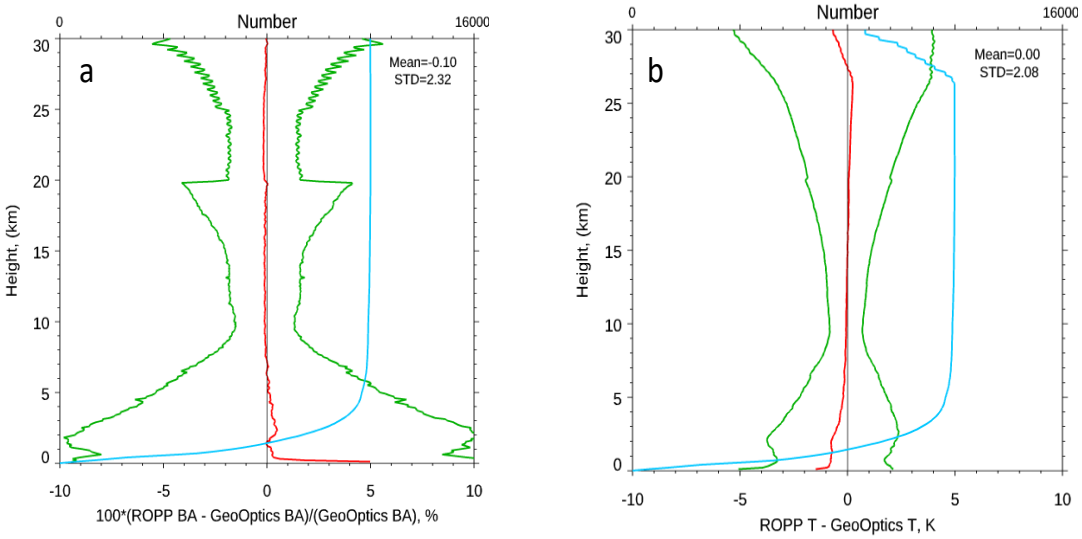

Figure 24 (a) the fractional bending angle difference between ROPP and GeoOptics and (b) temperature difference between ROPP and GeoOptics Comparison between GeoOptics Data and GFS 6-hour Forecast

7.4 **Improving the Extreme Weather Prediction in the Moisture Lower Troposphere using COSMIC GPS RO Measurements: Recent Case Studies**

In addition to the RO impacts on global NWP, COSMIC RO data are also very useful in improving the moisture and wind predicting for extreme weather using regional forecast models. In this section, we focus on recent developments of RO observational studies on extreme weather prediction such as atmospheric rivers and heavy rainfall events. Note that in the current NCEP operational NWP systems the RO bending angle observation errors (BAOE) are pre-defined using statistical approaches. However, because the RO bending angel measurement uncertainties are mainly caused by the combined effects of (i) lower signal-to-noise ratio (SNR), (ii) large vertical refractivity gradients, and (iii) possible violation of local spherical symmetry caused by the small-scale refractivity irregularities because of convection, they are highly location and season dependent.

The BAOE for each individual RO profiles and their location and seasonal variation may not been fully represented by the pre-defined BAOE. A current approach to estimate a proxy COSMIC BAOE based on individual observation local spectral width (LSW) is available recently. A case study of the impact of the LSW-based DBAOEs for COSMIC RO data on Tropical Cyclones (TC) prediction using the NCEP *Gridpoint Statistical Interpolation (GSI) and Global Forecast System (GFS)* is also presented.

The accurate estimate of individual COSMIC BAOE is also critical for improving water vapor prediction in the lower troposphere. Recently an approach to estimate a proxy COSMIC BAOE estimate based on individual observation local spectral width (LSW) was available from the COSMIC Data Analysis and Archive Center where each RO profile has an estimate of error at each level. To demonstrate how COSMIC RO data with the knowledge of available LSW-based BAOE can improve track and intensity prediction, Zhang et al., (2019) used the LSW-based DBAOEs for COSMIC RO data for Sinlaku Tropical Cyclones (TC) prediction using the NCEP *GSI and GFS.*

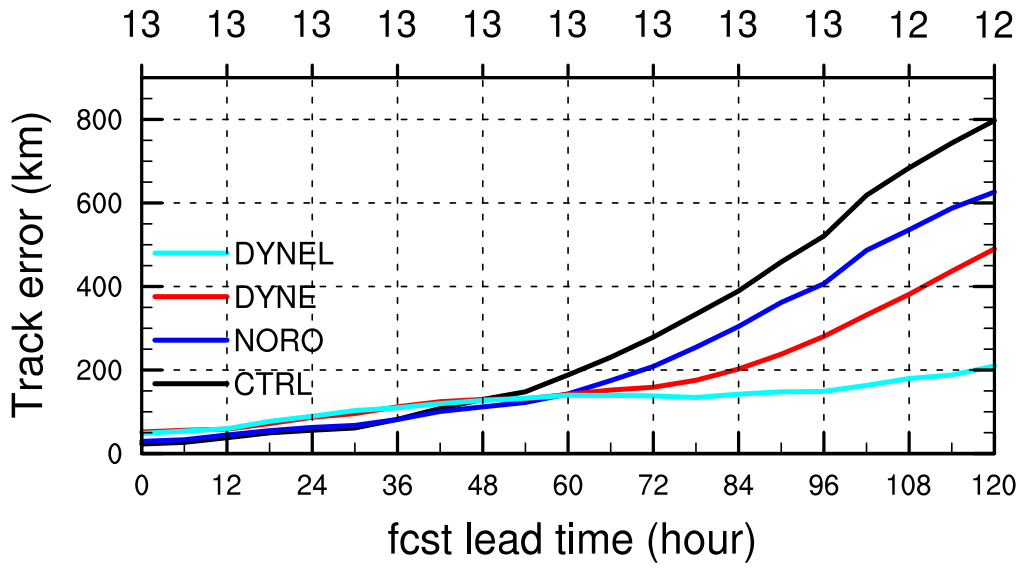

Fig. 25. The mean TC track prediction error. In the reference case (DYNE), the DBAOE equals to the LSW/2. A lower estimate (DYNEL) of 0.5 times the reference is also tested. The control (CTRL) used the current NCEP pre-defined statistical DBAOE.

Figure 25 shows that the application of the LSW-based dynamic bending angle error (DYNE) can greatly improve the track prediction in the 4-5 days forecast. The DYNE is equal to LSW/2. COSMIC data with LSW estimated BAOEs improve the simulation of the environment flows that steers the storm's movement significantly. In addition, the dynamic BAOEs also help improve the simulation of the fields of temperature, moisture and wind, providing favorable environment for Sinlaku's northwestward motion.

7.5 Using RO data to correct global radiosonde systematic temperature biases in the upper troposphere and lower stratosphere

Radiosonde observations (RAOBs) have provided long-term global *in situ* temperature, moisture, and wind measurements in the troposphere and lower stratosphere since 1958. However, because the quality of RAOB data vary with sensor types and heights, it is very difficult to use historical RAOB data to construct consistent temperature climate data records. The objectives of this study are to use consistently reprocessed GPS RO temperature data to characterize i) solar zenith angle (SZA) dependent temperature biases, ii) potential residual temperature errors due to incomplete radiation correction, iii) temperature biases due to change of radiation correction over different geographical regions, iv) the inter-seasonal and inter-annual variability of these temperature biases, and v) the trends of these biases and their uncertainty for different senor types in the upper troposphere and lower stratosphere.

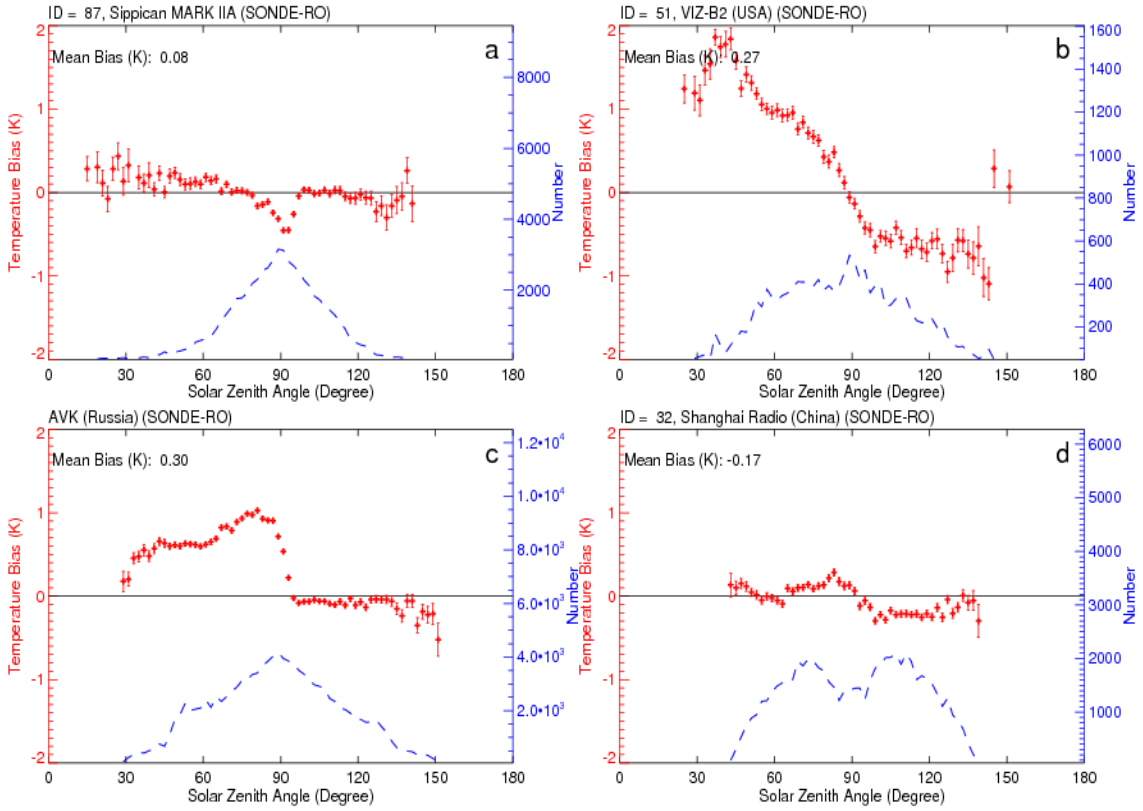

Figure 26. The mean temperature biases at 50 hPa varying for SZA from 0 degrees to 180 degrees for a) Sippican over United States minus RO, b) VIZ-B2 over United States minus RO, c) Russian Sonde minus RO, d) Shanghai minus RO. Only bins for more than 50 RAOB-RO pairs are plotted.

In this study, we use GPS RO temperature data from COSMIC, CHAMP, Metop-A and Metop-B consistently processed by UCAR CDAAC to identify the systematic temperature biases for different radiosonde temperature sensors in the upper troposphere and lower stratosphere. The precision of GPS RO is as small as 0.05 K in the UTLS. Because the quality of RO data does not change during the day or night and is not affected by clouds, the RO temperature profiles co-located with RAOBs are useful to identify the variation of temperature biases over time of different temperature sensors.

Fig. 26 depicts the mean temperature biases at 50 hPa varying for SZA from 0 degrees to 180 degrees for a) Sippican over United States minus RO, b) VIZ-B2 over United States minus RO, c) Russian Sonde minus RO, d) Shanghai minus RO. **Fig. 26** shows that different sensors contain different systematic biases relative to those of collocated RO temperature during the daytime and nighttime. The VIZ-B2 sonde has a large warm bias (as high as 2.0 K) during daytime and a cold bias (as low as -1.0 K) at night. While its nighttime biases are close to zero, AVK has a bias from about 0.7 K to 1.1 K in the daytime. Because the quality of RO temperature is not affected by sunlight, the small but obvious geographic-dependent biases are most likely due to the residual

radiation correction for these sensor types. This research was published recently in 2017 (Ho et al., 2017).

7.6 Initial Retrievals Results from the combined RO-AIRS and RO-MW Measurements

In this study, we use GPS RO data to constrain the AIRS temperature retrievals serving to improve moisture retrievals in the upper troposphere and lower stratosphere (UT/LS). In the upper troposphere, GPS RO refractivity is very sensitive to temperature but less sensitive to moisture. It is demonstrated that GPS RO refractivity can resolve temperatures greater than 1 K around 200 hPa but it can only sense about 15% of water vapor variation. **Figure 27** shows the temperature and moisture retrieval RMSE for AIRS, AMSU and, GPS RO as well as the combined AIRS, AMSU, and GPS RO data.

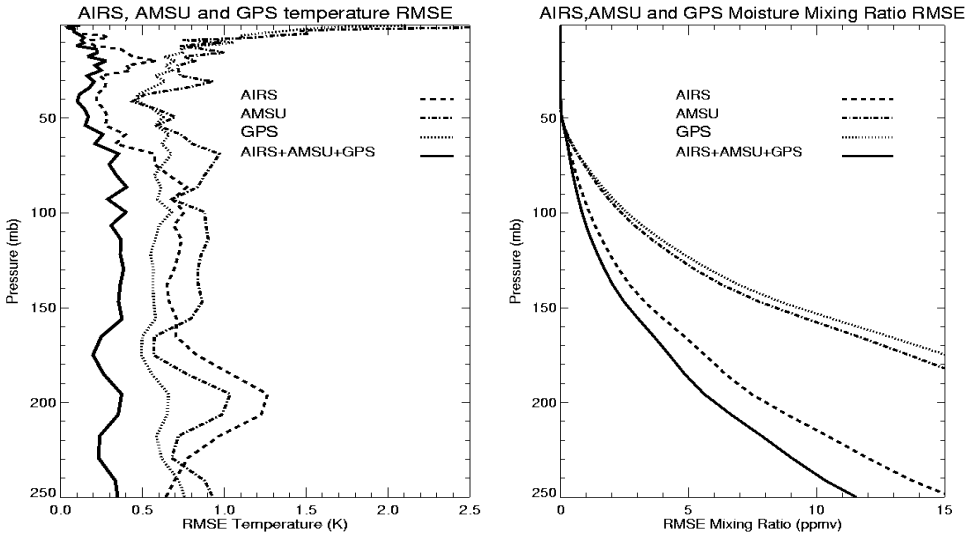

Fig. 27. The RMSE of temperature for AIRS, AMSU, GPS, and AIRS+AMSU+GPS in the UT/LS is on the left panel, and the RMSE of water vapor for AIRS, AMSU, GPS, and AIRS+AMSU+GPS in the UT/LS is on the right panel.

The multi-variable regression method is used for the data from the simulation study. The 100 level AIRS vertical grids are used for all AIRS, AMSU, and GPS RO data. With very high vertical resolution GPS RO refractivity profiles, AIRS and AMSU temperature RMSE are improved from 0.8 K and 1.0 K, respectively, between 250 hPa to 100 hPa (tropopause layer) to 0.4 K, which lead to AIRS and AMSU moisture RMSE around the same layer decrease from 4 ppmv and 15 ppmv, respectively, to around than 3 ppmv.

We have successfully implemented the RO refractivity forward operator into the current MiRS Version 11. This initial experiment is to demonstrate the feasibility of the proposed fusion approach to simultaneously retrieving global temperature and water profiles and hydrological data products using MiRS from the current operational COSMIC and ATMS data. Ten days of COSMIC-ATMS pairs are collected and inverted using RO-MiRS. **Figures 28 and 29** compared the co-located COSMIC and ATMS pairs (collected within 100 km and 15 minutes) with those temperature and moisture measurements from the Vaisala R92 radiosondes, respectively. **Figure**

28 depicts that the mean temperature biases for RO/ATMS relative to those from RS92 are equal to 0.39 K with a standard deviation of 2.26K for clear ocean cases and 0.0 K with a standard deviation of 2.35 K for cloudy ocean cases, respectively. The temperature biases for RO/ATMS results are larger from those over land than from those over oceans for both clear and cloudy conditions.

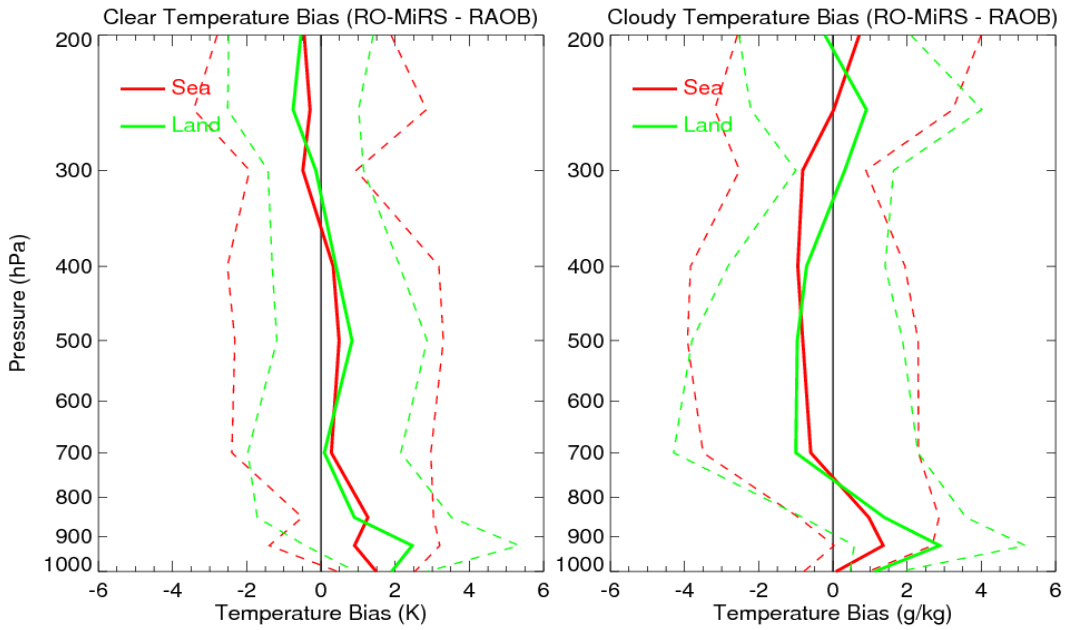

Figure 28. RO-MiRS COSMIC/ATMS retrieved temperature bias with respect to co-located RS92 measurements (red: ocean, green: land) for clear (left) and rainy (right) conditions.

Figure 29 shows comparison results for RO/ATMS global water vapor retrievals. Over ocean surfaces, the retrieved bias is relatively low at all layers. The land retrievals show a larger bias than those over oceans. The global mean water vapor biases from surface to 200 mb for clear/sea, clear land, cloudy/sea and cloudy/land cases are (0.11, 0.17, 0.11, 0.11) g/kg, respectively. The temperature and water vapor biases for ATMS-only retrievals relative to those from RS92 are about 10% to 20% larger than the COSMIC/ATMS results at different levels (not shown).

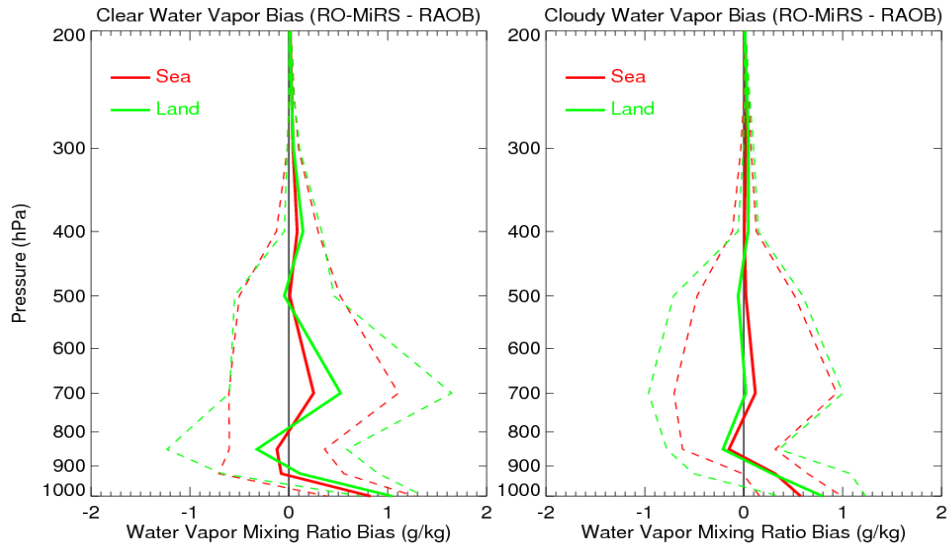

Figure 29. RO-MiRS COSMIC/ATMS retrieved water vapor bias with respect to co-located RS92 measurements (red: ocean, green: land) for clear (left) and rainy (right) conditions.

In the combined RO and AIRS retrieval (RO-AIRS), the high vertical resolution RO retrieved temperature profiles are able to help to resolve the sharp temperature inversion layer in the UT/LS (i.e., the tropopause) and constrain AIRS water vapor retrieval in the same altitude. Because RO data are also very sensitive to water vapor variation in the moisture rich troposphere, the RO data shall also help to provide extra water vapor information for the combined AIRS and RO retrievals in the lower troposphere. It is demonstrated that the combined AIRS and RO observations act to constrain the individual solutions, the significantly improved water vapor RMSE is found in both the middle and lower troposphere. The RMSEs of water vapor mixing ratio for AIRS and GPS RO are improved from 1.5 g/kg and 1.0 g/kg at surface, respectively, and to 0.5 g/kg for the GPS RO combined AIRS retrievals. Since GPS refractivity is less sensitive to temperature in the troposphere, only small temperature RMSE improvements are found. Similar results are found in the COSMIC, ATMS, ATMS+COSMIC retrieval results.

8. Summary of STAR Coordinated Activities, Community Services, Presentations, and Publications

8.1 Highlights of STAR's collaboration with national and international partners and community Service

There are a number of new projects / programs where STAR is significantly involved in the exploitation of their RO data: these are from partners' missions (KOMPSAT-5, PAZ, Metop, Metop 2nd Gen, Sentinel-6, etc).

STAR is also leading the effort to further explore the optimal approaches for using RO data in

the operational Data Assimilation (DA) environment through a Technology Maturation Project (TMP) RO project.

We have established an internal NOAA website to summarize activities, publication, and The current development on RO inversion package in

https://www.star.nesdis.noaa.gov/smcd/ncc/GNSSRO/GNSSRO_Publications/index.php

The login name is “cosmic”, the password is also “cosmic”

The National and international collaborations and Community Service since April 2019 conducted by STAR lead and team members are listed below.

- Work closely with OPPA on organizing the IROWG GNSS RO conference EUMETSAT on CWDP data evaluation
- Work closely with IROWG, G-VAP, SPARC, GCICS MW team, etc to promote interagency/international collaboration
- AMS 2020 special GNSS RO section chair
- AGU 2019 special GNSS RO section chair (working with JPL, UCAR and other agencies to organize this special section)
- Remote Sensing Guess editor
- SPARCS STAR lead
- GCISC RO lead in STAR
- G3 RO lead in STAR
- IROWG STAR lead
- TAO editor for COSMIC-2 special issue
- Co-chair of the WCRP (World Climate Research Program) SPARC global temperature profile climate record assessment.
- Member of the IROWG ROtrend working group: participate the ROtrend tele-conference meetings and work with other ROtrend members to quantify the structural uncertainty for RO data.
- Co-Principal Investigator for SCOPE-CM project: Sustained generations of upper tropospheric humidity (UTH) from multi-sensors with multi-agency cooperation, SCOPE-CM (Sustained and coordinated processing of Environmental Satellite data for Climate Monitoring).
- Member of the WCRP (World Climate Research Program) SPARC global temperature profile climate record assessment group.
- Provided text/presentation material on COSMIC, KOMPSAT-5, and RO water vapor sensing to Jack Kaye for CGMS meeting.
- Journal paper review: review RO-related journal papers from JGR, IEEE remote sensing, AMT, ACP, Journal of Radio science, etc.
- NOAA climate contact for COSMIC
- NASA atmospheric sounding Instrument and Science Team, Member
- NCAR SOARS steering committee: review panel members to select SOARS summer students for 2016.

8.2 List of STAR RO Presentations in Conferences and Workshops

We have given more than 15 presentations to summarize our C2 retrieval and validation results in national and international WS and conference since April 2019.

2020 (AMS)

- Shu-pen Ben Ho & Xinjia Zhou. (2020). COSMIC-2 Product Validation at NESDIS/STAR Using Global Radiosonde Observations. *American Meteorological Society*, Boston, MA, January 12-16, 2020
- Bin Zhang & Shu-pen Ben Ho. (2020). Error Assessments in the GNSS Radio Occultation Excess Phase/Bending Angle Calculation. *American Meteorological Society*, Boston, MA, January 12-16, 2020
- Changyong Cao & Shu-pen Ben Ho. (2020). The Significant Roles of COSMIC2 GNSS RO in NOAA Integrated Calibration/Validation System for NWP. *American Meteorological Society*, Boston, MA, January 12-16, 2020
- Erin Lynch & Flavio Iturbide-Sanchez. (2020). Intercomparison of Hyperspectral Infrared Sounders with Simulated Radiances from GNSS-RO Inputs *American Meteorological Society*, Boston, MA, January 12-16, 2020
- Xinjia Zhou & Shu-peng Ben Ho. (2020). NOAA Integrated Cal/Val System (ICVS) for Radio Occultation Performance Monitoring and Data Quality Assurance *American Meteorological Society*, Boston, MA, January 12-16, 2020

2019 (IROWG)

- Shu-pen Ben Ho & STAR GNSS Team NOAA/STAR. (2019). Inter-comparison between GNSS RO and hyperspectral infrared soundings and Combined Retrieval Results. *International Radio Occultation Working Group(IROWG)*, Konventum, Helsingør (Elsinore), Denmark, September 19-25, 2019
- Shu-pen Ben Ho & Xinjia Zhou. (2019). NESDIS RO Science Studies and Quality Assurance through the STAR Integrated Cal/Val System: Initial Validation of COSMIC-2 Data. *International Radio Occultation Working Group(IROWG)*, Konventum, Helsingør (Elsinore), Denmark, September 19-25, 2019
- Joint Center for Satellite Data Assimilation and CDAAC, STAR, OPPA. (2019). Commercial Weather Data Products Evaluation preliminary results. *International Radio Occultation Working Group(IROWG)*, Konventum, Helsingør (Elsinore), Denmark, September 19-25, 2019
- Xinjia Zhou & Shu-pen Ho. (2019). Construction of Temperature Climate Data Records using Multiple RO Missions. *International Radio Occultation Working Group(IROWG)*, Konventum, Helsingør (Elsinore), Denmark, September 19-25, 2019
- Bin Zhang & Shu-peng Ho, Xi Shao, Changyong Cao. (2019). Using Radio Occultation Profiles to Detect Microwave Sensor Bias for Climate Studies. *International Radio Occultation Working Group(IROWG)*, Konventum, Helsingør (Elsinore), Denmark, September 19-25, 2019

- Francois Vandenberghe& Suryakanti Dutta, Hailing Zhang, Hui Shao and James Yoe. (2019). Recent and New GNSS-RO missions: Quality Assessment and Comparative Data Assimilation. *International Radio Occultation Working Group(IROWG)*, Konventum, Helsingør (Elsinore), Denmark, September 19-25, 2019
- Stanislav Kireev & Shu-peng Ho. (2019). NOAA/STAR 1D-Var Retrieval Algorithm to Process Radio Occultation Data. *International Radio Occultation Working Group(IROWG)*, Konventum, Helsingør (Elsinore), Denmark, September 19-25, 2019

2019 (AGU)

- Shu-peng Ho & Xinjia Zhou. (2019). Climate Correction of Radiosonde Temperature Biases in the Lower Stratosphere using GPS RO data. *American Geophysical Union(AGU)*, San Francisco, CA, USA, December 9-13, 2019

Presentations in COSMIC-2 cal/val meetings:

- Ho, S.-P., et al., COSMIC-2 RO Products Validation using Satellite and In Situ Data, College Park, Sep. 10-11, 2019.
- Ho, S.-P., et al., Validation of COSMIC-2 Neutral Atmospheric Data Products using Measurements from Multiple Satellite Sensors and In situ Data, College Park, Taipei, Oct. 18-20, 2019.
- Ho, S.-P., et al., Validation of COSMIC-2 Neutral Atmospheric Data Products using In situ Data, San Francisco, CA, USA, Dec. 8, 2019.
- Ho, S.-P., et al., COSMIC-2 Product Validation at NESDIS/STAR Using Global Radiosonde Observations. *American Meteorological Society*, Boston, MA, January 12-16, 2020.

NOAA STAR team have published about 15 papers in world famous journals to summarize our inversion and validation results to demonstrate the maturity of our algorithms using other RO missions (i.e., COSMIC) as COSMIC-2 proxy data. We are preparing another four or five papers to summarize our COSMIC-2 results.

8.3 List of STAR Journal Papers

Paper have been published or under review:

1) Cao, Changyong, Wenhui Wang, Erin Lynch, Yan Bai, **S.-P. Ho**, 2020: Simultaneous Radio Occultation for Inter-satellite Comparison of Bending Angles towards More Accurate Atmospheric Sounding, Remote Sensing.
2) Steiner, A. K., F. Ladstädter, **S.-P. Ho**, 2020: Observed temperature changes in the troposphere and stratosphere from 1979 to 2018, J. of Climate.
3) Schröder, M., R. Bennartz, **S.-P. Ho,** 2020: Using GPS RO data as on-orbit references to calibrate Temperature in the Lower Stratosphere obtained from Satellite Microwave Sounders: Recent Results, GEWEX News letter.
4) Von Engeln, X., H. Gleisner, **S.-P. Ho**, A. Stanier, H. 2020: IPCC AR5 GPS RO section. (submitted).

5) Mears C., **S.-P. Ho**, J. Wang, H. Huelsing, and L. Peng, 2020: Total Column Water Vapor, [In "States of the Climate in 2018]. *Bul. Amer. Meteor. Sci.*, **98** (8), S24-S25, doi:10.1175/2019BAMSStateoftheClimate.1 State of the Climate.
6) Vinay Kumar; S. B. Surendra Prasad; K. Krishna Reddy; S. K. Dhaka; R. K. Choudhary; M. Venkatarami Reddy; **Shu-Peng Ho**, 2020: Temperature perturbations in the troposphere and lower stratosphere over a semi-arid region during the 2010 solar eclipse, PAAG-D-19-00515.
7) Li, ying, G. Kirchengast, B. Scherllin-Pirscher, M. Schwaerz, J. K. Nielsen, T.-K Wee, **S.-P. Ho**, and Y.-B. Yuan, 2019: new algorithm for the retrieval of atmospheric profiles from GNSS radio occultation data in moist air and cross-evaluation among processing centers, *Remote Sens.* **2019**, *11*(23), 2729; doi:10.3390/rs11232729
8) A. K. Steiner, F. Ladstädter, C. O. Ao, H. Gleisner, **S.-P. Ho**, D. Hunt, T. Schmidt, U. Foelsche, G. Kirchengast, Y.-H. Kuo, K. B. Lauritsen, A. J. Mannucci, C. Marquardt, J. K. Nielsen, W. Schreiner, M. Schwärz, S. Sokolovskyi, S. Syndergaard, A. von Engeln, J. Wickert, Consistency and structural uncertainty of multi-mission GPS radio occultation records, Atmos. Meas. Tech. Discuss., doi:10.5194/amt-2019-358
9) Mears C., **S.-P. Ho**, J. Wang, H. Huelsing, and L. Peng, 2019: Total Column Water Vapor, [In "States of the Climate in 2019]. *Bul. Amer. Meteor. Sci.*, **98** (8), S24-S25,doi:10.1175/2017BAMS State of the Climate
10) **Ho, S.-P.**, Achieving interoperability between Global Navigation Satellite System (GNSS) and GSICS: using GPS-RO as an on -orbit reference for Microwave Satellite sounders, GSICS News letter, doi: 10.25923/j01d-g110, Vol.13 No 1, 2019.
11) Yunheng Xue, Jun Li, W. Menzel Paul, Eva Borbas, **Shu-Peng Ho**, and Zhenglong Li, 2018: Impact of Sampling Biases on the Global Trend of Total Precipitable Water Derived from the Latest 10-Year Data of COSMIC, SSMIS and HIRS Observations, JGR (accepted).
12) **Ho, S.-P.**, R. A. Anthes, C. O. Ao, S. Healy, A. Horanyi, D. Hunt, A. J. Mannucci, N. Pedatella, W. J. Randel, A. Simmons, A. Steiner, F. Xie, X. Yue, Z. Zeng, 2019: The COSMIC/FORMOSAT-3 Radio Occultation Mission after 12 years: Accomplishments, Remaining Challenges, and Potential Impacts of COSMIC-2, *Bul. Amer. Meteor. Sci.,* DOI: 10.1175/BAMS-D-18-0290.1
13) **Ho, S.-P.**, Anthes, R. A., Zhang, H., Chen, S., 2019: Improving the Impact of Radio Occultation Observations on Numerical Forecasts of Tropical Cyclones, JCSDA Quarterly Newsletter, No. 62, Winter 2019, pp11-17. doi:10.25923/w2dh-ep66.
14) Vandenberghe, F., Shao, H., Dutta, S., Zhang, H., Ruston, B., McCarty, W., Ho, S., Cucurull, L., Yoe, G. J., 2019: Global Navigation Satellite Systems Radio Occultation Data Assimilation at JCSDA, JCSDA Quarterly Newsletter, No. 62, Winter 2019, pp7 - 11. doi:10.25923/w2dh-ep66.
15) Mears C., **S.-P. Ho**, J. Wang, H. Huelsing, and L. Peng, 2019: Total Column Water Vapor, [In "States of the Climate in 2018]. *Bul. Amer. Meteor. Sci.*, **98** (8), S24-S25, doi:10.1175/2017BAMS State of the Climate.

Papers are in preparation:

1) Shao. S., S.-P. Ho, COSMIC-2 Radio Occultation data quality evaluation through collocation-based and O-B inter-comparison

2) Shao. S., S.-P. Ho, Inter-calibration between COSMIC-2 Radio Occultation and SNPP and NOAA-20 CrIS through Radiative Transfer Modeling.

3) Shao. S., S.-P. Ho, Inter-comparison of COSMIC-2 Radio Occultation Retrieval Data with SNPP and NOAA-20 ATMS Measurements through Radiative Transfer Modeling

4) Kireev, S., and S.-P. Ho, COSMIC-2 1D Var inversion algorithm Water Vapor Retrievals in Tropical Moisture troposphere, Remote Sensing.

5) Adhikari, L. and S.-P. Ho, Inverting COSMIC-2 Phase Data to Bending Angle and Refractivity Profiles using the Full Spectrum Inversion Method, Remote Sensing (ready to submit).